

# 2016

## LPI SUMMER INTERN PROGRAM IN PLANETARY SCIENCE

*Papers Presented at the*

32nd Annual  
Summer Intern Conference

August 11, 2016 - Houston, TX



*Papers Presented at the*

# **Thirty-Second Annual Summer Intern Conference**

**August 11, 2016  
Houston, Texas**

2016 Summer Intern Program for Undergraduates  
Lunar and Planetary Institute

Sponsored by  
Lunar and Planetary Institute  
NASA Johnson Space Center



Compiled in 2016 by  
Meeting and Publication Services  
Lunar and Planetary Institute  
USRA Houston  
3600 Bay Area Boulevard, Houston TX 77058-1113

The Lunar and Planetary Institute is operated by the Universities Space Research Association under a cooperative agreement with the Science Mission Directorate of the National Aeronautics and Space Administration.

Any opinions, findings, and conclusions or recommendations expressed in this volume are those of the author(s) and do not necessarily reflect the views of the National Aeronautics and Space Administration.

Material in this volume may be copied without restraint for library, abstract service, education, or personal research purposes; however, republication of any paper or portion thereof requires the written permission of the authors as well as the appropriate acknowledgment of this publication.

## HIGHLIGHTS

---

### Special Activities

Date	Activity	Location
June 6	Lunar Curatorial and Stardust Lab Tour	NASA JSC
June 14	Mission Control	NASA JSC
June 19	Ice Cream Social	USRA
July 9	Murder Mystery Party	USRA
July 22	Robotics Systems Technology Branch Visit	NASA JSC
July 26	Meteorite Tour	NASA JSC
August 6	SkyFest	USRA
August 8	Director Sit Down	USRA
August 8	USRA Employee, Family, and Interns BBQ Picnic	USRA

### LPI Summer Intern Program 2016 — Brown Bag Seminars

*Wednesdays, 12:00 noon–1:00 p.m., USRA/Lunar and Planetary Institute*

Date	Speaker	Topic	Location
June 8	David “Duck” Mittlefehldt	Mafic Achondrite Meteorites and the Igneous Evolution of Asteroids	Hess Room
June 15	Cyrena Goodrich	Primitive Achondrites-Not Quite Chondrites, Not Quite Achondrites	Hess Room
June 22	Elizabeth “Liz” Rampe	Mars Curiosity Rover	Hess Room
June 29	Steve Clifford	Radar Investigations of Water on Mars	Hess Room
July 6	Paul Niles	Exploration Opportunities in Cislunar Space	Hess Room
July 13	LPI Interns	Mid-Term Reports	Hess Room
July 20	Allan Treiman	Venus	Hess Room
July 27	David Kring	Chicxulub Crater and Extinction of the Dinosaurs	Hess Room
August 2	Astronaut Don Pettit	Life on the Space Frontier	Hess Room
August 3	Patricia Craig	Identifying Potential Biosignatures on Mars	Hess Room
August 10	Paul Spudis	The Value of the Moon	Hess Room



## **LPI Summer Intern Tag Up and Science Fiction Film Series**

*Thursdays, 6:30 p.m., USRA/Lunar and Planetary Institute*

<b>Date</b>	<b>Title</b>	<b>Location</b>
June 9	Fish Story	Hess Room
June 16	Europa Report	Hess Room
June 23	The Core	Hess Room
June 30	The Fifth Element	Hess Room
July 7	Safety Not Guaranteed	Hess Room
July 14	Pitch Black	Hess Room
July 21	The Monolith Monsters	Hess Room
July 28	Edge of Tomorrow	Hess Room
August 11	The Martian	Hess Room

## AGENDA

---

8:00 a.m. **BREAKFAST**

8:25 a.m. Introductory Remarks by Drs. Stephen Mackwell, Paul Spudis, and Dave Draper

8:30 a.m. **KATIE BELL, Imperial College London**  
Advisors: Walter Kiefer and Matt Weller  
*Thermal Support of the Devana Chasma Rift, Venus* [#4003]

8:50 a.m. **SHANNON BOYLE, Rutgers University**  
Advisors: Cyrena Goodrich and Allan Treiman  
*Origin of Calcic Plagioclase in Polymict Ureilites* [#4002]

9:10 a.m. **MICHAEL CATO, Western Carolina University**  
Advisors: Justin Simon and Ryan Zeigler  
*Macro Textural Analysis of the Primitive Ordinary Chondrite NWA 5717* [#4005]

9:30 a.m. **SCOTT ECKLEY, University of Tennessee, Knoxville**  
Advisors: Paul Niles and Shawn Wright  
*The Effect of Shock on the Amorphous Component in Altered Basalt* [#4011]

9:50 a.m. **HUNTER EDWARDS, Virginia Polytechnic Institute and State University**  
Advisor: Patricia Craig  
*Insights into the Early Geologic Era of Mars Through Acid-Sulfate Vapor Weathering of Phyllosilicates* [#4012]

10:10 a.m. **LIAM HOARE, University of Bristol - Currently on a year abroad at Rutgers University**  
Advisors: David Kring and Martin Schmieder  
*LL-Chondrite Northwest Africa 6813: Sampling an Impact-Cratered Asteroid* [#4009]

10:30 a.m. **BREAK**

10:40 a.m. **ZOE HODGES, Durham University**  
Advisor: David "Duck" Mittlefehldt  
*Petrology of Igneous Clasts in Howardite Meteorites* [#4010]

11:00 a.m. **RUSHANA KARIMOVA, Jacobs University Bremen**  
Advisors: Georgiana Kramer and Erika Harnett  
*Correlating Swirls with Particle Tracking Simulations at Lunar Magnetic Anomalies in South Pole-Aitken Basin and Mare Crisium* [#4006]

11:20 a.m. **COLLEEN LAIRD, Case Western Reserve University**  
Advisor: Marc Fries  
*Analyzing North American Meteorite Falls to Develop a Mass Prediction Method Using NOAA RADAR Reflectivity Data* [#4008]

- 11:40 a.m. **CALDER PATTERSON, Carleton University**  
Advisor: Virgil “Buck” Sharpton  
*Reassessing the Size and Morphology of the Haughton Impact Structure* [#4004]
- 12:00 p.m. **SARAH PERRY, Vassar College**  
Advisor: Elizabeth “Liz” Rampe  
*Identifying Partially Chloritized Smectite at Gale Crater, Mars* [#4007]
- 12:20 p.m. **ERIC SCHMIDT, Embry-Riddle Aeronautical University**  
Advisor: Paul Spudis  
*Geological Map of the Humboldtianum Basin and Its Deposits* [#4001]
- 12:40 p.m. **LUNCH**

## CONTENTS

---

Thermal Support of the Devana Chasma Rift, Venus <i>K. L. Bell, W. S. Kiefer, and M. B. Weller</i> .....	1
Origin of Calcic Plagioclase in Polymict Ureilites <i>S. Boyle, C. A. Goodrich, and A. H. Treiman</i> .....	4
Macro Textural Analysis of the Primitive Ordinary Chondrite NWA 5717 <i>M. J. Cato and J. I. Simon</i> .....	7
The Effect of Shock on the Amorphous Component in Altered Basalt <i>S. A. Eckley, S. P. Wright, P. B. Niles, and E. B. Rampe</i> .....	10
Insights into the Early Geologic Era of Mars Through Acid-Sulfate Vapor Weathering of Phyllosilicates <i>H. R. Edwards and P. I. Craig</i> .....	13
LL-Chondrite Northwest Africa 6813: Sampling an Impact-Cratered Asteroid <i>L. Hoare, M. Schmieder, and D. A. Kring</i> .....	16
Petrology of Igneous Clasts in Howardite Meteorites <i>Z. V. Hodges and D. W. Mittlefehldt</i> .....	19
Correlating Swirls with Particle Tracking Simulations at Lunar Magnetic Anomalies in South Pole-Aitken Basin and Mare Crisium <i>R. Karimova, G. Y. Kramer, and E. M. Harnett</i> .....	22
Analyzing North American Meteorite Falls to Develop a Mass Prediction Method Using NOAA RADAR Reflectivity Data <i>C. E. Laird and M. D. Fries</i> .....	25
Reassessing the Size and Morphology of the Haughton Impact Structure <i>C. W. Patterson and V. L. Sharpton</i> .....	28
Identifying Partially Chloritized Smectite at Gale Crater, Mars <i>S. E. Perry and E. B. Rampe</i> .....	31
Geological Map of the Humboldtianum Basin and Its Deposits <i>E. F. Schmidt and P. D. Spudis</i> .....	35



# THERMAL SUPPORT OF THE DEVANA CHASMA RIFT, VENUS

K. L. Bell<sup>1</sup>, W. S. Kiefer<sup>2</sup>, M. B. Weller<sup>2,3</sup>

<sup>1</sup>Imperial College London, South Kensington, London SW6 2BP, Katie.bell13@imperial.ac.uk, <sup>2</sup>Lunar and Planetary Institute, 3600 Bay Area Blvd, Houston, TX 77058, kiefer@lpi.usra.edu <sup>3</sup>Department of Earth Science, Rice University, Houston, TX 77005, matt.b.weller@rice.edu

## Introduction:

The focus of this study was Beta Regio and the Devana Chasma rift on Venus. Beta Regio is a 2000 x 2500 km wide, 4 km high topographic rise [1] that is widely believed to be formed by an upwelling mantle plume [1-4]. This is demonstrated by the positively correlated, large amplitude gravity and topography signals [3] and extensive shield volcanism. Devana Chasma lies between Beta Regio and Phoebe Regio, which is another region of uplift directly south of Beta Regio. The mantle upwelling at Phoebe may be less active than at Beta as it is believed to be an older plume [5]. It is believed that Devana, which reaches depths of 3.3 km, is directly linked to the formation of Beta and Phoebe, with extension forming as a result of uplift [2, 6]. Devana has similar mechanics and characteristics to continental rift systems on Earth, like the African rift [7]. As shown in **Figure 1**, Devana Chasma is split into two distinct arms. These two segments may be a result of two different adjoining rift systems, with the northern and southern sections originating from Beta and Phoebe Regio respectively [6]. At the tip of the separate rifts, the stress fields interact causing the noticeable curvature. Surrounding the rifts there are regions of tesserae, commonly found on Venus, where the crust has been extensively deformed and thickened.

Previous studies have used flexural modelling of topography profiles [4, 8] and models of the relationship between gravity and topography [4, 9, 10] to determine the thickness of the elastic lithospheric ( $T_e$ ) at rift systems, volcanic rises, and coronae on Venus.  $T_e$  can then be related to the lithosphere's thermal gradient and heat flux [11].

This work used Magellan altimetry data for Devana Chasma and a lithospheric flexure model to determine how  $T_e$  varies along the rift. Our objective was to assess how heat flow varied with distance from the Beta Regio and Phoebe Regio convective upwellings and to use this data to improve our knowledge of mantle plume dynamics on Venus. Previous work used just 1 or 2 profiles to assess lithospheric structure across broad regions of Venus [4]. Our study looked at profiles spaced every ~100 km along the rift to obtain a

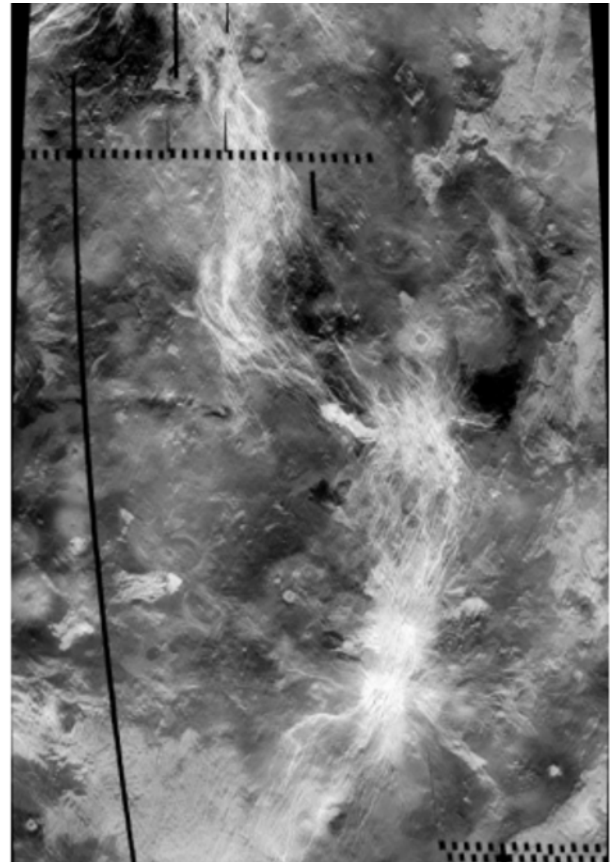


**Figure 1:** Radar image of Devana Chasma extending between Beta and Phoebe Regio. The bright regions show areas of roughness, commonly due to tectonic faulting. Dark areas are smooth, such as pahoehoe lava flows [6].

higher resolution and better understanding of the lithospheric structure.

## Method:

The flexure profiles were modelled based on the equation for elastic flexure of a line load [12]:

$$w(x) = d_1 \exp\left(-\frac{x}{\alpha}\right) \cos \frac{x}{\alpha} + d_2 \exp\left(-\frac{x}{\alpha}\right) \sin \frac{x}{\alpha} + d_3 x + d_4 \quad (1)$$

where  $w$  is the flexural topography induced by the lithospheric load  $d_1$  and  $d_2$ . For the Devana rift, the load comes from normal faulting, which creates a central



rift valley by crustal thinning, which in turn leads to flexural uplift of the rift flanks.  $d_3$  is the regional slope, and  $d_4$  is the topographic regional mean. The flexural parameter,  $\alpha$ , is a function of  $T_e$ , and  $x$  is the position along the profile. This specific solution to the flexure equation models linear loading when the load is applied exclusively at the origin. Non-zero values of  $d_3$  and  $d_4$  indicate that part of the topography has a non-flexural origin. This may be a strong influence in Devana due the association with the mantle plumes beneath Beta and Phoebe Regio.

A five dimensional grid search code has been developed to explore combinations of the flexural parameters and  $T_e$  for a given profile; 25 profiles were tested in total. The fit between the profile and the model is assessed using the Root Mean Square (RMS) misfit; the best-fit values are those corresponding to the minimum misfit. An example of a best-fit model is illustrated in **Figure 2**. The eastern and western sides of the profiles are tested independently; this method avoids the central depression of the rift, and offers an additional constraint on the model results. The relationships between parameters in Eq. 1 contain information regarding the structure of the lithosphere, e.g. whether the lithosphere is broken or continuous. If  $d_1=d_2$  the implication is that of a continuous lithosphere and in the condition where  $d_1 \neq d_2$  and  $d_2=0$  this indicates that the lithosphere is broken [12]. The Magellan altimetry data has an estimated uncertainty of about 20 m for this latitude range on Venus [13, 14]. The uncertainty of the best-fit parameters is estimated by looking at the range of values that fit the data with RMS misfits within 20 m of the minimum misfit.

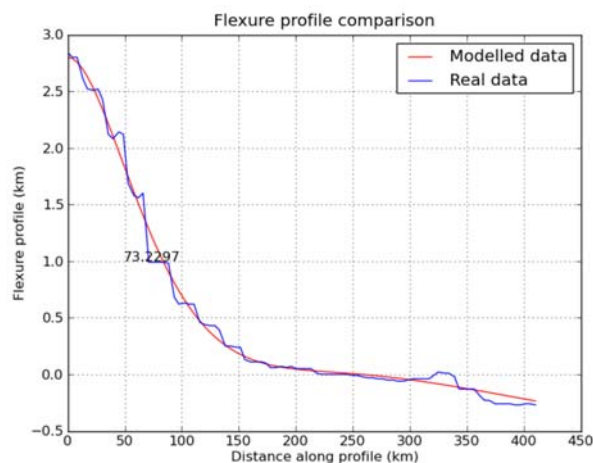


**Figure 2:** Profile 16° N, eastern flank. This graph shows the fit between the model parameters and the altimetry profile. The misfit between data and model is 73 m. This model clearly fits well with the profile, and the noise on the data is small.

In some cases, it was also found that the flexure model had difficulty in fitting large areas of noise or topographic features. As seen in **Figure 1** along the south eastern edge of the rift there is a large bright area, which is believed to be tesserae. This feature creates an increase in crustal thickness at the end of most of the eastern profiles. Tesserae are thought to be regions of thickened crust; therefore, in an attempt to mitigate its affect, selected profiles have been clipped to remove the anomalous region. Further, many of the profiles in the south eastern side were not tested because the extent of deformation of the rift axis was so severe, the model would not be able to fit the profile.

### Results:

$T_e$  is a function of the thermal structure of the lithosphere, therefore it should vary smoothly with distance and have similar values on the east and west sides of the rift. In our model  $T_e$  values range from 4 km to 89 km along the rift. These values change rapidly with distance and are often significantly different on the east and west flanks of the rift. These observations suggest that the elastic flexure model (Equation 1) only explains part of the observed topography and thus cannot be used to derive constraints on the lithospheric thermal gradient and heat flux. This observation was only possible because our study modelled a large number of profiles along the rift. This further suggests that studies examining a single transect and extrapolating those results to the rift systems as a whole, may be misleading [e.g., 4].

**Figure 3** shows the relationship between  $d_4$  and position along rift. Both the eastern and western flanks (red and blue lines, respectively in Fig. 3) show a high degree of correlation. The graph indicates a decreasing trend as the rift moves away from Beta Regio to a minimum at  $\sim 10^\circ$  N, corresponding to the region of rift arm interaction, after this point the value of  $d_4$  begins to increase again. A plausible interpretation is that for Devana Chasma,  $d_4$  is measuring topography which is thermally supported by upwelling mantle convection. The trend of the  $d_4$  graph indicates that the rift system lies between two mantle plumes. Interestingly, values of  $d_4$  in the southern region, near Phoebe Regio, are similar to those near Beta Regio, in the North, despite Phoebe being thought to be an older plume [5]. Instinctively it might be expected that there would be less dynamic support as a result of the greater age. Furthermore the lack of correlation between the values of  $T_e$  on either side of the rift could imply that the dynamic support beneath the rift is asymmetric.

In the analytic flexure model for a line load [12],  $d_1=d_2$  occurs when the elastic lithosphere is continuous beneath the rift, which is usually the case in this study. Although many faults are visible in Figure 1, they ap-

parently do not fully penetrate the lithosphere in most cases. Alternatively, if  $d_2=0$ , this indicates a broken plate, in which faulting completely penetrates the lithosphere. Our results show that this occurs in some localized regions of Devana Chasma.

#### Conclusions:

This work has enabled further understanding of the lithosphere on Venus. It has been found that dynamic support from convection plays a more significant role than simple lithospheric support in Devana Chasma. Furthermore it has been found that lithospheric thickness is not consistent along the rift; there are large variations and gradients between measurements and on either side of the rift, which suggests that any dynamic support is asymmetric. There is also evidence for localised broken lithosphere.

#### Future work:

Similar models are currently being developed for the Ganis Chasma rift in Atla Regio to test if the same relationships apply at other rifts on Venus. Further work will need to be conducted to understand the relationship between the dynamic topography and the heat flux of planet. This may include analysing models of mantle plume dynamic uplift [3] with the flexure model (Equation 1), as well as gravity models of litho-

spheric structure in Devana and Ganis, similar to those of [15] for other regions of Venus.

#### References:

- [1] Basilevsky and Head (2007), *Icarus*, 192, 167-186.
- [2] Stofan et al. (1989), *Geological Society of America Bulletin*, 101, 143-156.
- [3] Kiefer and Hager (1991), *Journal of Geophysical Research*, 96, 20,947-20,966.
- [4] Barnett et al (2002), *Journal of Geophysical Research*, 107, No E2.
- [5] Kiefer and Peterson, *Geophys. Res. Lett.* 30, 2002GL015762, 2003.
- [6] Kiefer and Swafford (2006), *Journal of Structural Geology*, 28, 2144-2155.
- [7] Nimmo and McKenzie (1996), *Earth and Planetary Science Letters*, 145, 109-123.
- [8] Johnson and Sandwell (1994), *Geophys. J. Int.*, 119, 627-647.
- [9] Simons et al (1997), *Geophys. J. Int.*, 131, 24-44.
- [10] Hoogenboom et al (2005), *Journal of Geophysical Research*, 110, E09003.
- [11] McNutt (1984), *Journal of Geophysical Research*, 89, 11,180-11,194.
- [12] Turcotte and Schubert (2002), *Geodynamics*, 2<sup>nd</sup> ed., Cambridge University Press, New York.
- [13] Rapaport et al., (1999), *Icarus*, 139, 19-31.
- [14] Ford and Pettengill, *Journal of Geophysical Research*, 97, 103-114.
- [15] Moore and Schubert (1997), *Icarus*, 128, 415-428.

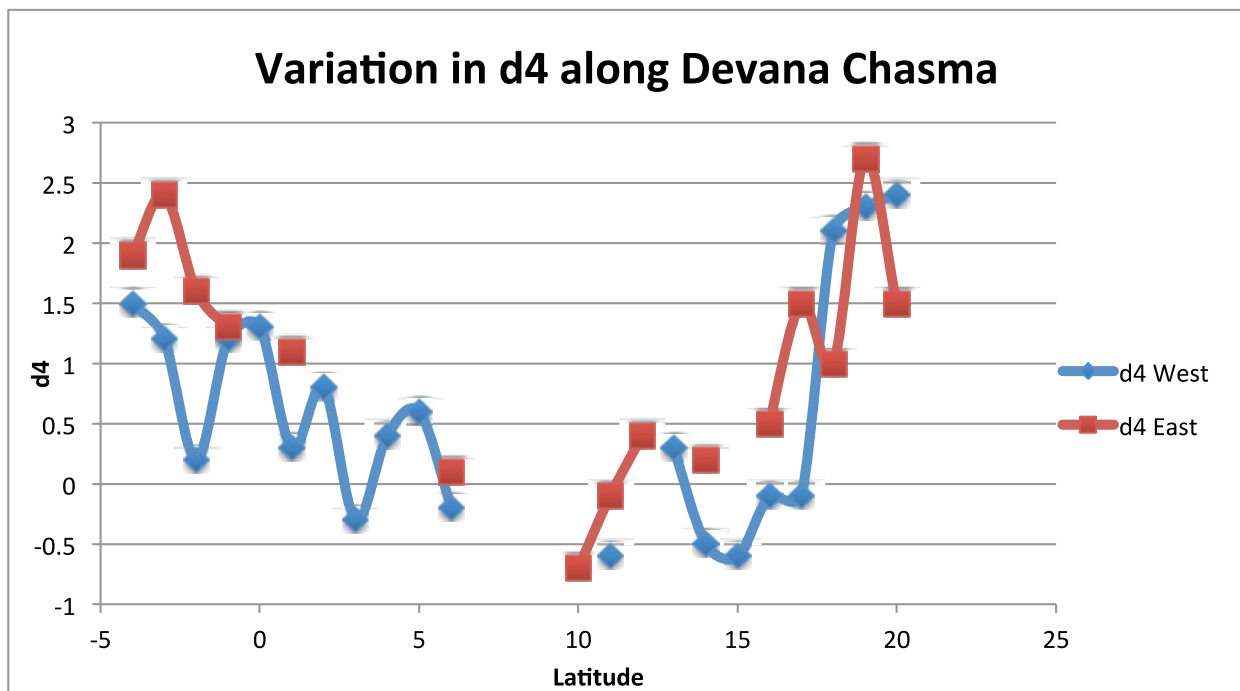


**Figure 3:** A graph showing the change in  $d_4$  with latitude along the rift. When  $d_4$  is large, it means that a substantial part of the topography has a non-flexural origin. The non-flexural topography decreases with increasing distance from Beta Regio (from 20 N to 10 N latitude) and also decreases with distance from Phoebe Regio (from 5 S to 7 N latitude). This is consistent with thermal support for part of the rift topography, because the thermal support would be expected to be largest beneath central Beta and central Phoebe, where the convective upwellings are most prominent. Error bars have not been included on the graph as the errors on these values are much smaller than the incremental values of the data.

**ORIGIN OF CALCIC PLAGIOCLASE IN POLYMICT UREILITES.** S. Boyle<sup>1</sup>, C.A. Goodrich<sup>2</sup>, and A.H. Treiman<sup>2</sup>, <sup>1</sup>Rutgers, the State University of New Jersey, 57 US Highway 1, New Brunswick, NJ 08901 USA, boyleshannonmarie@gmail.com, <sup>2</sup>Lunar & Planetary Institute, Houston, TX.

**Introduction:** Ureilites are the second largest group of achondritic meteorites. They are dominated by olivine and pyroxene, with other minor phases, such as carbon, metals, and sulfides [1,2]. Normal ureilitic material represents the residual mantle of an asteroid that has undergone partial differentiation [3]. Polymict ureilites are breccias representing the regolith of the ureilite parent body [3,4]. They have inclusions of other meteorite types, as well as plagioclase (Figure 1). Previous studies argue that these plagioclase clasts represent two, distinct ureilitic melt lithologies; one with “albitic” plagioclase ( $An = \text{molar } Ca/(Ca+Na+K) = 0-32$ ) and another with “labradoritic” plagioclase ( $An 33-69$ ) [3]. This paper discusses the origin of highly calcic plagioclase grains, defined as  $An 70-100$ , in two polymict ureilites, DaG 999 and NWA 10657. In addition, comparisons will be made between the calcic clasts of this study and a unique, ungrouped achondrite, NWA 7325, which also contains highly calcic plagioclase [5,9,14]. Our goal is to determine whether these clasts are ureilitic or foreign.

**Method:** The JEOL 7600F field emission scanning electron microscope (FESEM) was used to obtain X-ray maps of the following elements in NWA 10657\_004, a previously unstudied sample: Al, Ca, Cl, Cr, Fe, K, Mg, Mn, Na, Ni, O, P, S, Si, and Ti (maps of DaG 999, NWA 10657\_MZ, and NWA 10657\_003 were provided by Goodrich). The FESEM was run at 15 keV and 30 nA on two weekends, providing five X-ray map sections of the sample. Individual element maps in each section were combined into a CMY map using ImageJ. Photoshop was then used to combine each of the five sections into a whole, composite image (Figure 1).

The JEOL 8530F field emission electron microprobe (EMPA) provided quantitative data for all thin sections. A complete survey of plagioclase clasts larger than 90 microns was conducted on samples DaG 999 (51 clasts) and NWA 10657\_004 (82 clasts). Four plagioclase clasts were analyzed in NWA 10657\_MZ and one in NWA 10657\_003. Initial surveys of the samples were run at 15 keV and 10 nA. For higher precision, the highly calcic plagioclase clasts were subsequently reanalyzed using 15 keV, 25 nA and longer count times for FeO and MgO. The oxide data generated by the probe were input into Excel for data processing.

**Results:** *General petrography.* The thin section NWA 10657\_004 is 690 mm<sup>2</sup> and represents a typical polymict ureilite [6]. Based on point counting conducted in ImageJ, the sample contains 1% feldspathic material (excluding chondritic clasts). Only four out of

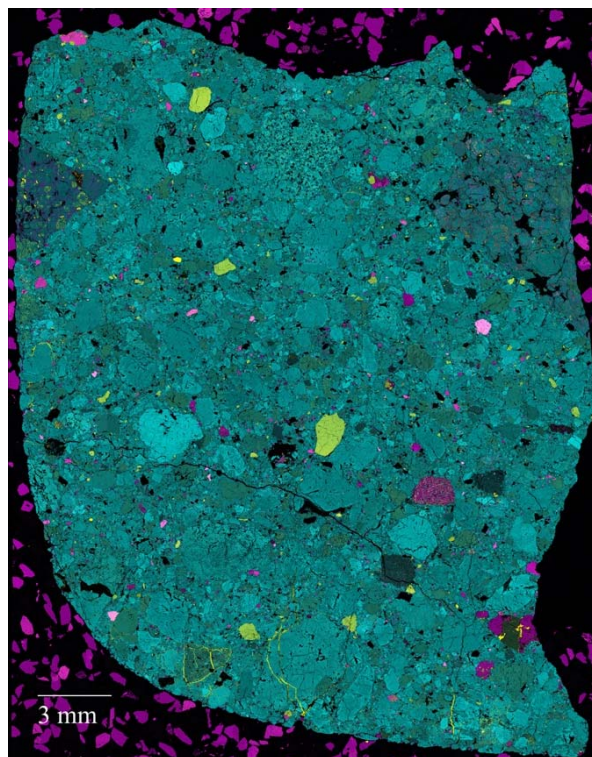


**Figure 1.** Cyan (Mg), magenta (Al), and yellow (Ca) X-ray map of NWA 10657\_004. The sample is primarily ureilitic olivine (cyan), with two large chondrites in the top half on either side, high Ca pyroxenes (lime), and small plagioclase grains (various pinks). High-Ca plagioclase grains are pale pink.

138 plagioclase clasts studied, in all four thin sections, contain primary mafic material. The remaining clasts consist of single fragments of plagioclase. A histogram of all plagioclase clasts studied is presented in Figure 2a. The figure is complemented by a histogram of work by [3] and [7] (Figure 2b). In previous work, the “albitic” lithology represented 66% of the plagioclase clasts, the “labradoritic” lithology represented 26%, and highly calcic plagioclase clasts represented 8%. Figure 2a shows a large increase in calcic plagioclase clasts; where 44% represent the “albitic” lithology, 24% represent the “labradoritic” lithology, and 32% represent highly calcic plagioclase clasts.

*Plagioclase composition.* Figure 3a is a plot of average FeO weight percent versus average An in each highly calcic plagioclase clast. Data collected in this study are in black. Plotted for comparison are angrite and NWA 7325 data [8,9,5]. Only four clasts from this study plot near NWA 7325 and two clasts from this study plot in the area of angrites.



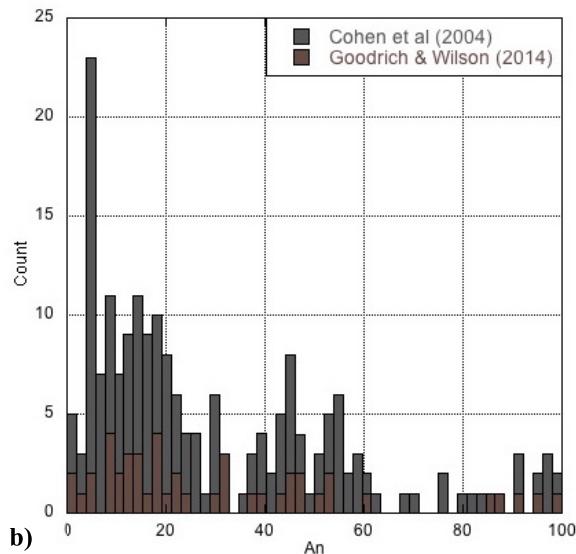
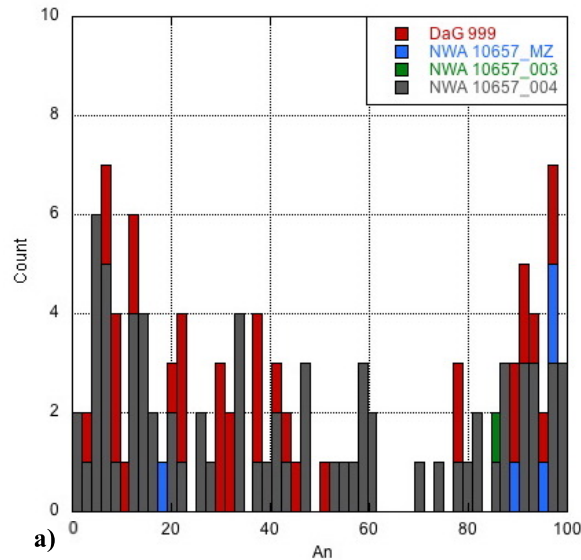


**Figure 2.** Histograms of average An content for each plagioclase clast in this study (a) and previous studies of plagioclase in polymict ureilites (b) [3,7].

Figure 3b is a plot of average MgO weight percent versus average An in each plagioclase clast. The majority of the clasts have MgO content similar to plagioclase in NWA 7325, as measured by [9], though [5] reports significantly higher values for MgO. Higher anorthite content slightly correlates with lower MgO weight percent, which tends toward angritic composition.

**Mafics.** There are four clasts that have mafic minerals in addition to the highly calcic plagioclase: clast 16 in DaG 999 and clasts 17, 53, and 81 in NWA 10657\_004. Figure 4 shows these clasts plotted with the

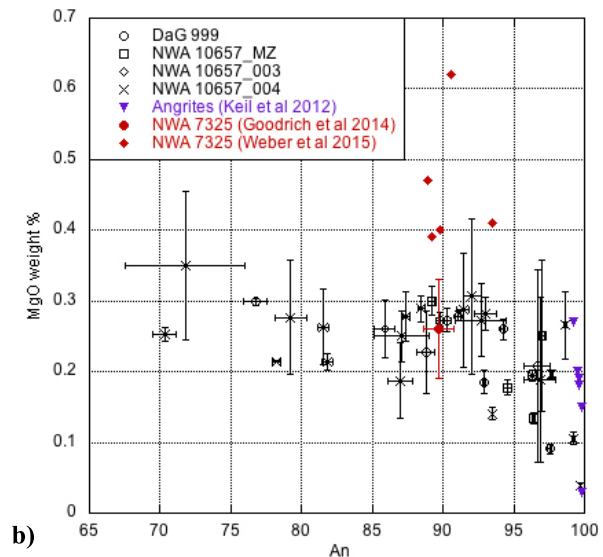
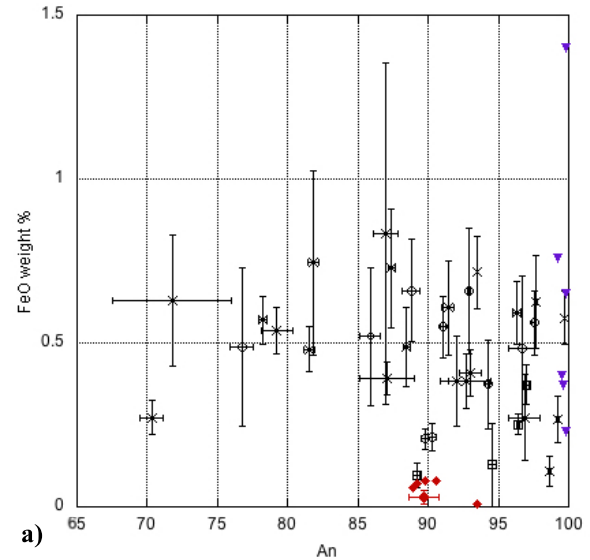


**Figure 3.** Scatter plots of average FeO and MgO weight percent versus average An content in highly calcic plagioclase clasts. Clasts from this study are in black, angrite data is in purple, and NWA 7325 data is in red [5,8,9].

major groups of anchondrites. Clast 53 in NWA 10657\_004 and clast 16 in DaG 999 plot near NWA 7325. The Wo content of pyroxene in clasts 53 and 16 also matches that of NWA 7325. Clast 17 in NWA 10657\_004 has lower An of plagioclase and Mg# of pyroxene, relative to NWA 7325. Clast 81 in NWA 10657\_004 displays a wide range of An content. However, even at its largest value, it is still lower than the An content of NWA 7325.

**Discussion:** This study shows that calcic plagioclase clasts (An 70-100) form a significant population in

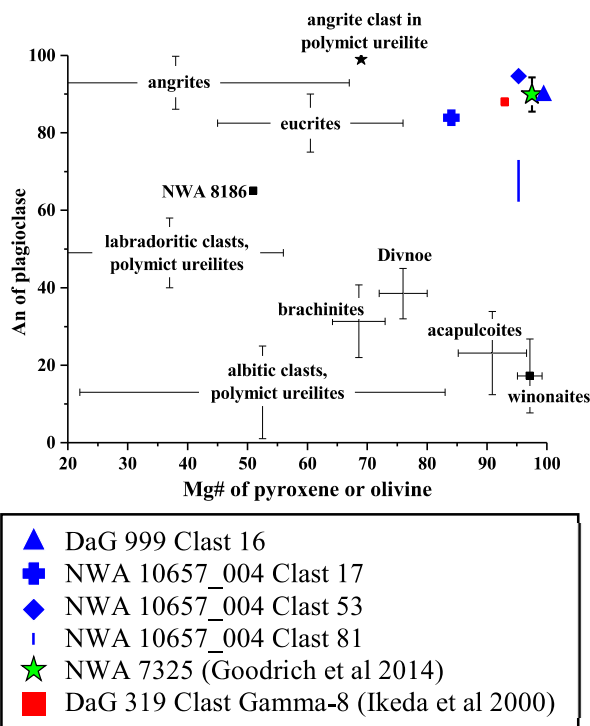


**Figure 2.** Plot of An of plagioclase versus Mg# of pyroxene or olivine. Supplementary meteorite data is provided for comparison. DaG 319 is a polymict ureilite [10,11]. Data for NWA 7325 is from [9] and the angrite clasts in polymict ureilites are from [12] and [13].

some polymict ureilites. Data from the 36 highly calcic plagioclase clasts studied indicates that there are no overall trends of varying FeO or MgO with An, suggesting multiple clast origins. Some of the most calcic clasts have compositions similar to angrites, which have been reported as foreign clasts in polymict ureilites [12, 13]. Oxygen isotope analysis could distinguish such clasts.

NWA 7325 consists of Ca-plagioclase (An~90), Mg-olivine (Fo~98), and Ca-Mg-pyroxene (mg#~98, Wo~45), which does not match any known meteorite [5,9,14]. However, [9] and [11] noted its similarity to some rare clasts in polymict ureilites (Figure 4). The plagioclase in NWA 7325 shows distinctive secondary remelting textures, with a complex assemblage of recrystallized phases (Figure 5b). Eleven of the calcic plagioclase clasts in this study show textures similar to the texture in NWA 7325 plagioclase (Figure 5a), yet only one of those eleven has An and FeO contents akin to NWA 7325. Possible conclusions include: 1) most of the calcic plagioclase clasts in polymict ureilites are not related to NWA 7325; 2) some of the calcic plagioclase clasts in polymict ureilites are pieces of NWA 7325-like meteorites and they are more varied in mineral composition than NWA 7325 itself; and/or 3) elements, such as FeO and MgO, were redistributed during secondary remelting in a way that is not yet understood.

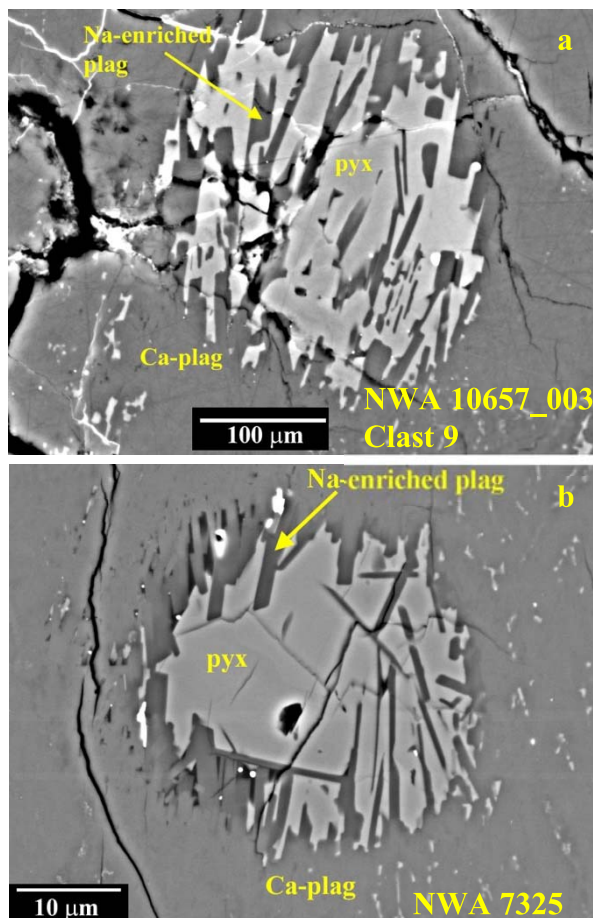


**Figure 5.** Backscatter electron images (BSE) of the unique texture in NWA 7325 and NWA 10657\_003.

Additionally, Figure 4 illustrates that NWA 7325 and these highly calcic plagioclase clasts in polymict ureilites are unique compared to other known meteorite types. Perhaps these six data points represent a previously unrecognized parent body. Future work on these samples will include oxygen isotope and trace element analysis and petrologic modeling.

**References:** [1] Goodrich C.A. (1992) *Meteoritics* 27, 327-352. [2] Mittlefehldt D.W., et al. (1998) *In Planetary Materials* (ed. J.J. Papike). Mineralogical Society of America. *Reviews in Mineralogy* 36, 195. [3] Cohen B.A., et al. (2004) *GCA* 68, 4249-4266. [4] Goodrich C.A., et al. (2004) *Chemie der Erde* 64, 283-327. [5] Weber I., et al. (2015) *MAPS* 51, 3-30. [6] *Meteoritical Bulletin Database*. [7] Goodrich C.A., Wilson L. (2014) *Lunar Planet Sci.* 45, #1342. [8] Keil K. (2012) *Chemie der Erde* 72, 191-218. [9] Goodrich C.A., et al. (2014) *Lunar Planet Sci.* 45, #1455. [10] Ikeda Y., et al. (2000) *Antarct. Meteorite Res.* 12, 177-221. [11] Kita N.T., et al. (2004) *GCA* 68, 4213-4235. [12] Prinz M. et al. (1986) *Lunar Planet. Sci.* 17, 681-682. [13] Goodrich C.A., et al. (2015) 78<sup>th</sup> MSM, #5048. [14] Irving A.J., et al. (2013) *Lunar Planet Sci.* 44, #2164.

# MACRO TEXTURAL ANALYSIS OF THE PRIMITIVE ORDINARY CHONDRITE NWA 5717. M. J.

Cato<sup>1,2</sup> and J. I. Simon<sup>2</sup>, <sup>1</sup>Geosciences and Natural Resources Dept., 331 Stillwell Building, Western Carolina Univ., Cullowhee, NC, 2872, USA, <sup>2</sup>Center for Isotope Cosmochemistry and Geochronology, ARES, NASA JSC, Houston, TX 77058, USA

**Introduction:** Northwest Africa 5717 is a very primitive (subtype 3.05) ungrouped ordinary chondrite which contains two apparently distinct lithologies. The darker of these, lithology A, looks to host the second, much lighter in color, lithology B. The nature of the boundary between the two is variable and at times uncertain, ranging from abrupt to gradational and not always following particle boundaries. The distinction between the lithologies, beyond the obvious color differences, has been supported by a discrepancy in oxygen isotopes and an incongruity in the magnesium contents of chondrule olivine [1].

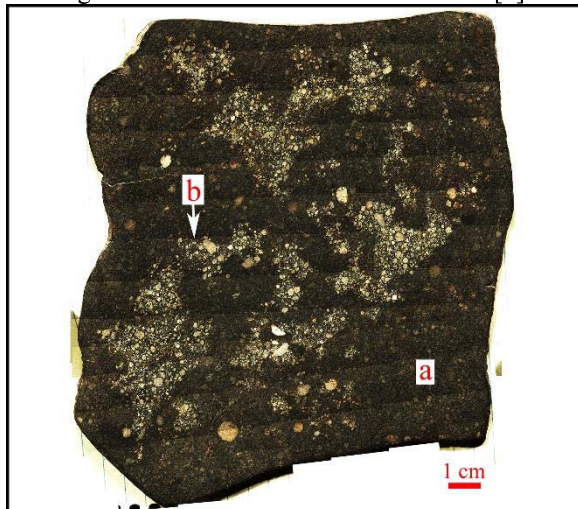


**Figure 1.** Low-resolution mosaic image of NWA 5717 slab. The dark lithology is denoted by (a) and light by (b).

The highly primitive nature of NWA 5717 along with the likelihood of it containing two distinct lithologies predicts that it likely records aspects of early asteroid parent body formation. Of apparent importance to planetesimal accretion models are the narrow particle size distributions reported for many undifferentiated chondrites [2]. Recent studies, however, have shown a conflicting broad particle size distribution in the well-known carbonaceous chondrite Allende [3,4].

Here, digital methods have been used to investigate the validity of the two apparent lithologies within NWA 5717, the particle size distribution, and presence of a penetrative petrofabric in order to address incongruities in previously published data and ultimately help understand the processes that occurred during the formation of these primitive chondrites.

**Procedure:** Particles from a high-resolution mosaic image of a roughly 13x15cm slice of NWA

5717 were traced in *Adobe Photoshop*. Due to the large size of the sample, visually representative regions of each lithology were chosen to be analyzed. The resulting layers of digitized particles were imported into *ImageJ*, which was used to measure their area, along with the axes, the angle from horizontal, and the centroid coordinates of ellipses fitted to each particle. Resulting 2D pixel areas were converted to spherical diameters employing the unfolding algorithm of [5], which outputs a 3D particle size distribution to fit the data. *Spatsat* was used to create kernel density plots of the centroid coordinates for each region. Data from previously digitized thin sections and a large slab of Allende [3] were used for comparison purposes.

**Results:** *Particle Size Distribution:* When comparing the size distribution obtained by digitizing high-resolution images of a large NWA 5717 slab to those from other chondrites analyzed using different methods, a significant systematic bias associated with these methods becomes apparent. As shown in Figure 2, the NWA 5717 data set, like a recent study of Allende [3], exhibits a broad size distribution that is distinct from those previously reported for the same or similar types of primitive meteorites [2,3,4].

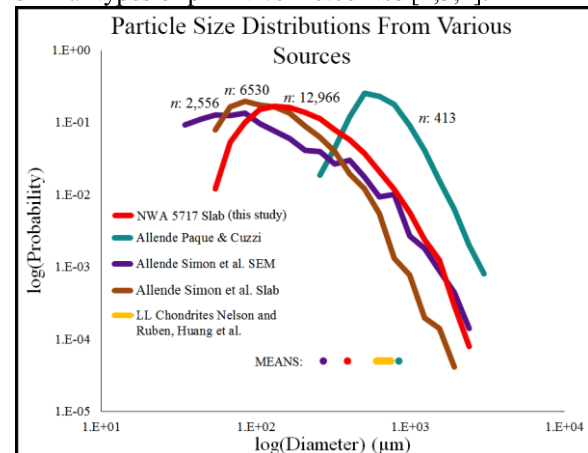


**Figure 2.** Log-log plot showing particle size versus normalized relative frequency for NWA 5717 (ordinary) and Allende (carbonaceous) chondrites. Paque & Cuzzi [4] measured disaggregated particles from bulk Allende material, Simon et al. [3] measured both scanning electron microscope X-ray image data obtain in thin sections and a high-resolution mosaic of a slab of Allende, and NWA 5717 was completed using high-resolution mosaics of a slab in this study. Published mean particle sizes of other chondrites measured by several methods are shown for reference [2].



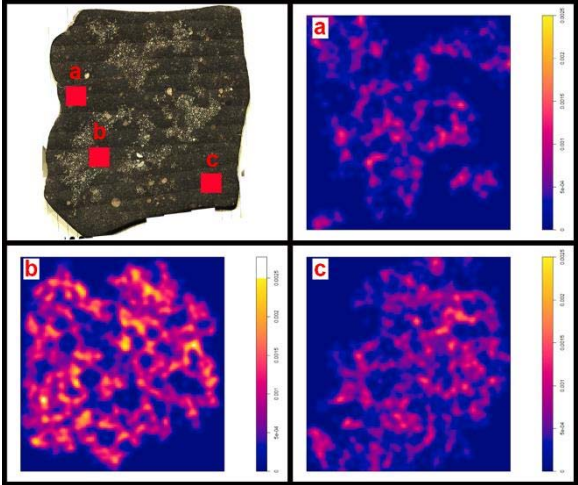
*Dual Lithologies:* The macro textural data produced in this study cannot confirm the presence of two distinct lithologies. As shown in Table 1, neither lithology differs greatly from the other in any textural aspect. While this difference appears to be significant, it becomes important to assess whether it is truly a result of separate lithologies or larger scale heterogeneity within the sample as a whole affecting individual digitized regions.

Sample Portion	Angle	Circular Diameter (μm)	Aspect Ratio	Volume % Particles
All measured	81.4 ±49.9	393±649	1.67±0.55	0.87
Dark	79.7 ±49.1	423±657	1.69±0.58	0.88
Light	84.4 ±51.1	337±644	1.64±0.50	0.85

	Core Fa	Rim Fa	Ferroan Ol Cr <sub>2</sub> O <sub>3</sub>	Δ <sup>17</sup> O
Dark	9.7-20.8	16.2-35.6	0.23-0.91	0.539, 0.554
Light	0.03-3.4	17.2-27.5	0.28-0.78	0.061, 0.080

**Table 1.** Comparison between proposed lithologies in NWA 5717. Angle from horizontal, circular diameter, aspect ratio, and volume percent means are a result of digitization. Core Fa, rim Fa, Cr<sub>2</sub>O<sub>3</sub>, and oxygen isotopes were reported in [1]. Angle from horizontal, circular diameter, and aspect ratio include standard deviation from the mean while Bunch et al. [1] data contains ranges and multiple measurements.



**Figure 3.** Kernal density plots of three regions within the slab of NWA 5717 with increasing density as the color shifts from blue to yellow. Regions (a) and (c) both contain only the dark and (b) is primarily the light lithology.

Figures 3 and 4 show some apparent particle size heterogeneity that spans the entire sample, but that it

is largely irrelevant of the lithologies within. The kernel density plots in Figure 3 along with the spread in Figure 4a confirm the existence of a particle size heterogeneity among individual digitized regions. The size distributions b and c in Figure 4, however, show that within individual digitized regions both the light and dark lithologies are indistinguishable. Due to the possibility of inconsistencies in sampling between regions affecting particle size distribution, regions that appeared to more significantly undersample the smallest size portions were omitted from Figure 4a.

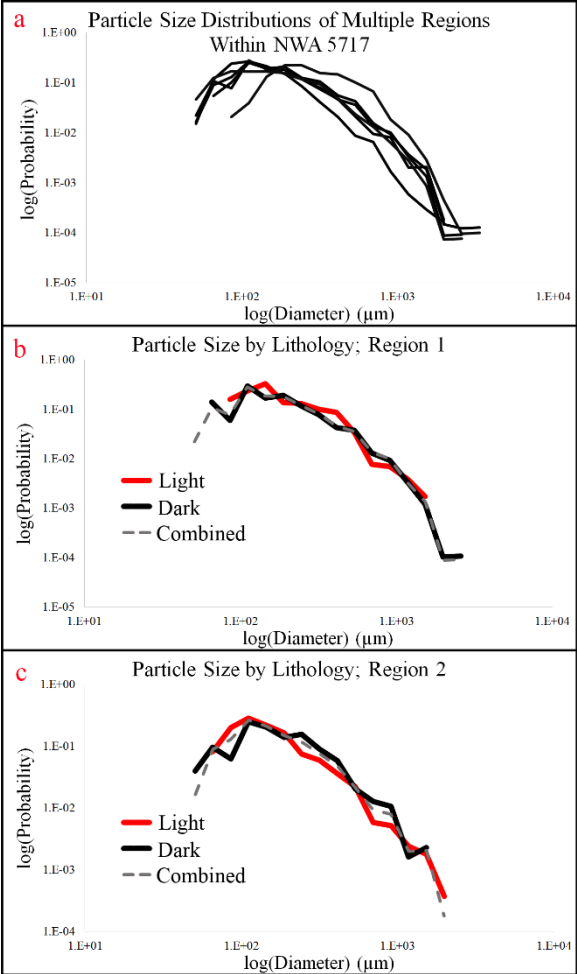


**Figure 4.** Log-log plot showing particle size versus normalized relative frequency. Chart (a) contains a suite of complete regions from across the sample, with (b) and (c) showing the breakdown between light and dark lithologies within two separate regions.

*Petrofabrics:* A strong penetrative fabric was observed in NWA 5717. With 12,327 particles measured, a strong preferred orientation of 81.4 (±49.9 SD) degrees from horizontal was evident. The two lithologies did not differ significantly from each other, with mean orientations only 4.7 degrees apart. The most significant distinction between the lithologies is

the profile of the angle distribution represented by the rose diagrams in Figure 5. The light lithology has a larger representation of particles oriented roughly 90 degrees from the preferred orientation, but not enough of the sample was digitized to eliminate the possibility that this heterogeneity was a result of location of the chosen regions within the sample or a specific function of two separate lithologies.

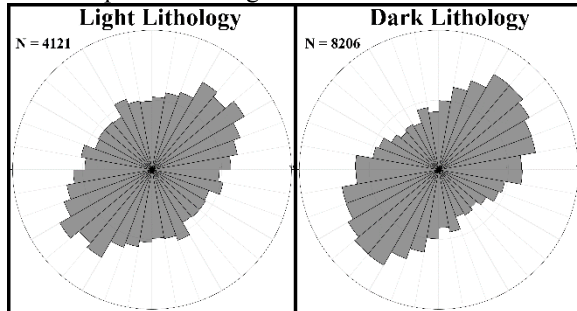


**Figure 5.** Rose diagrams of the angle from horizontal of particles in NWA 5717 binned at 10°. The dark and light lithologies are separated with N representing total number of particles in the given rose diagram.

**Discussion:** *Particle Size Distribution:* The differences shown between differing sampling methods in Figure 2 are too significant to purely be a result of heterogeneity within the meteorite; the Paque & Cuzzi sample would have to be almost completely void of the <600µm fraction seen in both the SEM and slab analyses by Simon et al. We propose that disaggregation destroys, or renders unmeasurable, this fine-grained fraction, creating a narrow distribution heavily weighted in the coarser sizes. A similar phenomena is observed when comparing data obtained through high-resolution photos of slabs, including NWA 5717, and that obtained through SEM analysis. The point where size undersampling starts to become apparent in both NWA 5715 and the Allende photomosaic is similar, between 100-200 µm, while SEM data appears to have minimal undersampling.

*Dual Lithologies:* While macro textural analyses did not confirm the presence of two separate lithologies, previous chemical studies by Bunch et al., as seen in Table 1, appear to show a difference between the two. A more detailed chemical and micro analysis of NWA 5717 would be beneficial to solidly confirm the presence of these two separate lithologies. Whether these two separate groups are a result of separate lithologies and/or are merely a product of alteration, this sample contains a litany of unanswered questions. Currently, plans have been made to run some diagnostic tests on the two lithologies. Within the next few weeks, spectrometry of both lithologies will be analyzed and a set of chemical X-ray maps will

be produced of a thin section containing both lithologies within the paired sample NWA 7402.

*Petrofabrics:* More focused analyses of NWA 5717 would be beneficial to understand the possible mechanism behind the formation of the penetrative petrofabric seen in the sample. Particle lineations have been observed in other primitive chondrites before, but they remain surprisingly understudied since such petrofabrics were first reported in the 1960s [6]. At this point, neither early accretionary processes, impact, nor gravitational overburden can be ruled out. Micro analyses to access possible shock affects in relation to both individual particle elongation and overall petrofabric orientation would be particularly beneficial. The relation between these three can be used to put together an overall deformation history for the sample. For example, if the orientation of shock affects are consistent with the elongation of individual particles, but not the overall petrofabric, it would suggest that the initial deformation of particles was a result of impact while another process, such as gravitational overburden, was the mechanism for the sample-wide fabric formation. The opposite can also be the case, if shock is consistent with the petrofabric orientation but not that of individual particle elongation, another mechanism, such as particle deformation during initial accretion, would have to be proposed to explain individual particle deformation.

**Conclusions:** Macro textural analysis of a large slab of NWA 5717 has proven to be a valuable method of assessing sample-scale textural features. We have shown that in chondritic samples, it can be used to quantify distributions of particle shape, orientation and distribution. When comparing the size distribution resulting from this method with those of a different chondrite analyzed using a range of methods, it appears to be likely that there is a significant systematic bias for many of the existing data. Despite macro textural analyses, NWA 5717 itself is still a mystery; these sample-scale textural analyses were unable to provide significant evidence for the presence of different lithologies, despite previous chemical analyses by Bunch et al. [1] More chemical and micro analyses will be needed to determine if the two observed lithologies are truly unique.

**References:** [1] Bunch T. E. et al. (2010) *LPSC IVI*, Abst. #1280. [2] Fredrich J. M. (2015) *chemie der erde*, 75, 419-443. [3] Simon, J. I. et al., (*unpublished data*). [4] Paque J. M. and Cuzzi J. N. (1997) *LPSC XXVIII*, Abst. #1189. [5] Cuzzi J. N. and Olson D. M. (2016) *MAPS*, accepted. [6] Dodd Jr, R.T. (1965) *Icarus*, 4, 308-316.

**THE EFFECT OF SHOCK ON THE AMORPHOUS COMPONENT IN ALTERED BASALT** S. A. Eckley<sup>1,2</sup>, S. P. Wright<sup>3,4</sup>, P. B. Niles<sup>5</sup>, and E. B. Rampe<sup>6</sup> <sup>1</sup>Planetary Geosciences Institute, Department of Earth and Planetary Sciences, University of Tennessee, Knoxville, TN 37996, USA (seckley@vols.utk.edu) <sup>2</sup>Jackson School of Geological Science, University of Texas, Austin, TX 78712, USA <sup>3</sup>Planetary Science Institute, Tucson, AZ 85719, USA <sup>4</sup>Department of Geology and Environmental Science, University of Pittsburgh, Pittsburgh, PA 15260, USA <sup>5</sup>Astromaterials Research and Exploration Science, NASA-Johnson Space Center, Houston, TX 77058, USA <sup>6</sup>Aerodyne at NASA-JSC, Jacobs-JETS Contract.

**Introduction:** Investigation of the geochemical and mineralogical composition of the Martian surface provides insight into the geologic history of the predominantly basaltic crust. The Chemistry and Mineralogy (CheMin) instrument onboard the Mars Science Laboratory (MSL) rover, Curiosity, has returned the first X-Ray diffraction data from the Martian surface [1]. However, large proportions ( $27 \pm 14$  with some estimates as high as 50 wt. % [1,2]) of an amorphous component have been reported. As a remedy to this problem, mass balance equations that couple Alpha Particle X-Ray Spectrometer (APXS) geochemistry, Sample Analysis at Mars (SAM) volatile chemistry, and CheMin mineralogy have been employed to constrain the geochemistry of the amorphous component [1,2]. However, “the nature and number of amorphous phases that constitute the amorphous component is not unequivocally known” [2]. Multiple hypotheses have been proposed to explain the origin of this amorphous component. Using XRD pattern fitting programs, [1] and [3] found allophane and basaltic glass were the best candidates for the amorphous phases. However, the geochemistry is not consistent with these conclusions. [1] argue that allophane “may be an XRD surrogate for another amorphous phase such as the  $\text{Fe}^{3+}$ -bearing phase hisingerite,” supporting the hypothesis that allophane could not exist as an amorphous phase due to the high  $\text{SiO}_2/\text{Al}_2\text{O}_3$  [4]. Glass, whether volcanic or impact induced, and/or its alteration product, palagonite, are agreed to be a prevalent amorphous phase in the global Martian dust [1,3,4,5]. Other geochemical indicators imply a S/Cl-rich component (i.e. amorphous sulfates or amorphous akaganeite) [1,2,4,5] and a  $\text{Fe}^{3+}$  nanophase ferric oxide component (npOx) could exist [1,4,5]. Establishing a multi-phase amorphous component from a basaltic precursor, that has undergone physical and chemical weathering within geochemical constraints, is of paramount importance to better understand the composition of a large portion of the Martian surface (up to 50 wt. %).

This paper focuses on shocked basalts from Lunar Crater in India, which are valuable analogs for the Martian surface, because it is a well-preserved impact crater in a basaltic target [6]. Having undergone pre- and post-shock aqueous alteration, these rocks provide crucial data regarding the effect of shock on the

amorphous component in altered basalt. By conducting similar mass balance equations, we attempt to calculate the geochemistry of the amorphous component in altered basalts ranging from unshocked to Class 5 (Table 1) [6]. This has the potential to reveal the nature and origin (i.e. primary igneous, shock metamorphic, and/or aqueous alteration occurring before or after the impact event) of the amorphous component in shocked basalt with the goal of unravelling the history of the Martian surface.

**Table 1:** *Classes of shocked basalt petrography (adapted from [6])*

Class	Shock	
	Pressure (GPa)	Petrographic Description
1	<20	Grains are fractured
2	20-40	Plagioclase transformed to maskelynite
3	40-60	Plagioclase transformed to a flowing glass of plagioclase composition
4	60-80	Plagioclase converted to vesicular glass; pyroxene melted on crystal edges and/or heavily fractured
5	>80	Plagioclase and pyroxene completely melted

**Methods:** Basaltic samples from the Lunar Crater, located within Deccan Traps, were acquired by Dr. Shawn Wright during multiple field seasons. Twenty-seven samples were chosen, representing a range of levels of alteration from unshocked/unaltered to Class 5 shocked basalt clasts [6], that were found along the crater walls and in the ~1 m thick suevite matrix surrounding the crater. We acquired whole rock geochemistry data from the XRF laboratory at Franklin and Marshall. Crushed rock powder ( $0.4000 \pm 0.0001$  grams) was mixed with lithiumtetraborate ( $3.6000 \pm 0.0002$  grams), placed in a platinum crucible and heated with a meeker until molten. The molten material was transferred to a platinum casting dish and quenched. This produced a glass disk that was used for XRF analysis. Powder XRD data were collected at NASA’s Johnson Space Center on a Panalytical X’Pert Pro diffractometer with Cu  $K\alpha$  radiation. All samples were

scanned from 2-75° 2 $\theta$ , with a step size of 0.02°. Crystalline phases and abundances were determined using HighScore Plus and Jade softwares' Rietveld refinement method; the amorphous abundance was determined by the internal standard method (sample mixed with 20 wt. % corundum).

**Mass-balance equations.** To quantify the amorphous component, we utilized a technique modeled after [5], where, simply put, we determine the difference in geochemistry between the bulk and crystalline to obtain the amorphous geochemistry.

$$\text{Oxide}_{\text{Bulk}} - [\text{Oxide}_{\text{Crystalline}}] = \text{Oxide}_{\text{Amorphous}}$$

$$\text{Oxide}_{\text{Bulk}} - [\sum y_m * x_m \text{ with } \sum x_m = 1] = \text{Oxide}_{\text{Amorphous}}$$

After retrieving specific chemical formulae for the crystalline phases, we calculated the elemental abundance (in wt. % oxide) ( $y_m$ ) in each mineral. Next, we calculated a weighted sum of each oxide in a given rock by multiplying the abundance of a given oxide in each mineral ( $y_m$ ) by the abundance of each mineral ( $x_m$ ) in the bulk rock (amorphous included). These weighted oxide sums were subtracted from the bulk oxide geochemistry to return the geochemistry, in wt. % oxide, of the amorphous component in each rock. Necessary corrections were used for negative amorphous values and these corrected values were renormalized (Table 3).

**Results and Discussion:** The XRD analyses indicated a variety of phases within the twenty-seven samples: andesine, augite, pigeonite, quartz/cristobalite, hematite, magnetite, ilmenite, calcite, zeolites, vermiculite, and a range of hydrated phyllosilicates. In addition to crystalline phases, a broad amorphous hump was reported for most rocks above the Class 1 shock level (Table 1). Samples LC04-056, LC09-235, LC09-

Phase	056 unshocked	235 Class 2	327 Class 3	05 Melt Class 5
Augite	26.6	47.4	26.6	8.5
Pigeonite	9.8	-	10.9	4.8
Calcite	-	-	6.7	-
Andesine	54.9	1.7	2.1	21.5
Ilmenite	0.7	-	2.1	-
Muscovite	-	18.3	-	-
Ferrosilite	-	-	0.9	-
Hematite	-	3.6	-	-
Magnetite	1.0	-	0.5	1.9
Quartz	-	-	0.3	-
Amorphous	7.0	29.0	49.9	63.3
Total	100	100	100	100

**Table 2:** Samples chosen for mass-balance calculations, from unshocked to Class 5, with phases and abundances (wt. %)

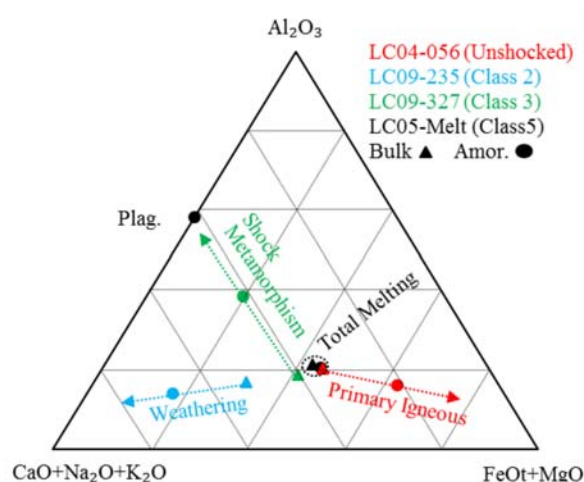
**Table 3:** Calculated oxide geochemistry (wt. %) for the crystalline and amorphous components, renormalized to 100 %

Oxide	LC04-056 (unshocked)		LC09-235 (Class 2)	
	Crystalline	Amorph.	Crystalline	Amorph.
SiO <sub>2</sub>	62.89	9.22	47.43	46.28
TiO <sub>2</sub>	0.30	7.97	0.51	3.29
Al <sub>2</sub> O <sub>3</sub>	13.24	16.99	15.93	9.60
FeO <sub>T</sub>	5.26	37.17	9.46	14.51
MnO	0.07	0.72	0.00	0.32
MgO	4.46	14.25	11.49	0.00
CaO	10.93	11.82	11.16	24.56
Na <sub>2</sub> O	2.85	0.00	1.03	2.35
K <sub>2</sub> O	0.00	1.01	3.00	0.00
P <sub>2</sub> O <sub>5</sub>	0.00	0.85	0.00	0.35
TOTAL	100.00	100.00	100.00	100.00

Oxide	LC09-327 (Class 3)		LC05-Melt (Class 5)	
	Crystalline	Amorph.	Crystalline	Amorph.
SiO <sub>2</sub>	46.94	49.69	51.24	50.48
TiO <sub>2</sub>	2.34	2.39	0.00	3.79
Al <sub>2</sub> O <sub>3</sub>	1.18	21.07	17.08	12.01
FeO <sub>T</sub>	14.55	13.11	9.58	16.39
MnO	0.00	0.35	0.00	0.31
MgO	14.27	0.00	5.81	4.92
CaO	20.40	9.54	13.28	9.32
Na <sub>2</sub> O	0.31	3.17	3.01	1.34
K <sub>2</sub> O	0.00	0.35	0.00	1.06
P <sub>2</sub> O <sub>5</sub>	0.00	0.33	0.00	0.37
TOTAL	100.00	100.00	100.00	100.00

327, and LC05-melt were selected for mass-balance calculations because they had the best fit refinement patterns. Table 2 reports the phases and abundances within samples that were used to calculate the geochemistry of their respective amorphous components (Table 3). Our analyses reported major crystalline phases of augite, pigeonite and andesine with average compositions of  $\text{Ca}_{0.88}\text{Mg}_{0.94}\text{Fe}_{0.18}\text{Si}_2\text{O}_6$ ,  $\text{Mg}_{0.85}\text{Fe}_{0.98}\text{Ca}_{0.17}\text{Si}_2\text{O}_6$ , and  $\text{Ca}_{0.48}\text{Na}_{0.52}\text{Al}_{1.4}\text{Si}_{2.6}\text{O}_8$ , respectively. The data from Table 3 were converted to molar % and plotted on an A-CNK-FM ternary diagram (Figure 1) [7] to illustrate mixing and weathering of primary igneous phases [8]. Mixing lines connect the bulk and respective amorphous geochemistry. These arrows represent the evolution of the amorphous component from the bulk geochemistry by various geologic processes. LC04-056 is an unshocked basalt with an amorphous percentage of 7 %, thought to be a



**Figure 1:** A-CNK-FM ternary diagram [7] with bulk and amorphous geochemistry (molar %) for the four calculated samples. Arrows represent the various processes by which amorphous components are derived in our basaltic samples.

primary feature that was formed during natural igneous processes (Figure 1). LC09-235 displays a weathering trend that is interpreted to be the result of pre- or post-shock alteration. Its bulk geochemistry trends towards the CNK apex, so it has undergone overall alteration. The impact event could have either shocked these secondary minerals to amorphousness or created micro-conduits [9] that exacerbated the formation of secondary minerals that are either poorly crystalline or near the limit of detection for our XRD analysis. LC05-melt shows homogenization of both the amorphous and crystalline components. This is expected with a Class 5 impact melt that has undergone total melting and conversion to almost two-thirds glass. Finally, LC09-327 has the most interesting process of amorphous component generation: shock metamorphism. This is a Class 3 shocked basalt where, according to [6], plagioclase is transformed beyond maskelynite into a flowing glass of plagioclase composition. The respective amorphous component lies directly on a mixing line between the bulk and plagioclase compositions. This amorphous component was created solely through the transformation of plagioclase into an amorphous glass of identical composition.

**Conclusions:** The goal of this research is to understand how impacting has contributed to the production of glass and perhaps alteration on the Martian surface. The high (50+ %) abundances of amorphous components we calculated from XRD analyses match previous petrographic analyses [6] that show this is the conversion of labradorite to various impact glasses (Table 1). Thus, plagioclase can be preferentially fractionated from the target rock during

an impact by being shocked or shock-melted to a glass to create an enrichment in plagioclase or plagioclase-composition glass in the amorphous component relative to unmelted pyroxene (Table 1). Therefore, if the Martian surface is globally homogenized by aeolian mixing [11], then it is safe to assume that a portion of the global dust could be derived from this shock-induced plagioclase-composition glass. Indeed, most impacting occurred in the first billion years of Martian history, but recent small craters could produce significant amounts of ejecta and other alteration products [12]. With these ideas, we hypothesized that the Rocknest amorphous component could be a mixture of shock-induced plagioclase composition glass (no more than 33%) and another amorphous weathering product. We found that mixing 69 wt. % of the residue created by [8] in their acidic weathering experiments of LA synthesized basalt with 31 % plagioclase composition glass would yield a geochemistry identical to the Rocknest amorphous component (Figure. 2). We assume that a portion of the LA residue would become amorphous after high pH and water/rock weathering. Whereas this hypothesis is based off many assumptions, it provides a groundwork for further research on how shock has effected the Martian surface.

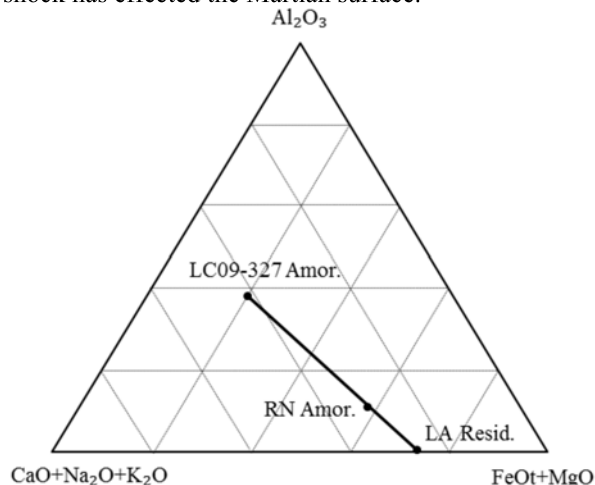


**Figure 2:** A-CNK-FM ternary diagram [7] illustrating the mixing between a shock-induced amorphous component (327) and an acidic weathering residue (5 wt. % FeTi-oxides added in) [8] to form the Rocknest amorphous geochemistry [10].

**References:** [1] Bish D. L. et al. (2013) *Science*, 341, 6153 [2] Morris R. V. et al. (2014) *LPSC 45 #1319* [3] Blake D. F. et al. (2013) *LPSC 44 #1289* [4] Morris R. V. et al. (2013) *LPSC 44 #1653* [5] Dehouck E. et al. (2014) *JGR 119*, 2640-2657 [6] Kieffer S. W. et al. (1976) *LPSC 7*, 1391-1412 [7] Nesbitt H. W. and Young G. M. (1982) *Nature*, 715-717 [8] Hurowitz J. A. et al. (2006) *JGR 111*, E2 [9] Wright S. P. (2013) *LPSC 44 #1010* [10] Blake D. F. et al. (2013) *Science*, 341, 1239505-1 – 1239505-7 [11] McSween H. Y and Keil K. (2000) *GCA*, 64, 2155-2166 [12] Burns R. G. (1993) *GCA*, 57, 4555-4574 [13] Reagan et al. (1996), *GSA* 302, 235-243 [14] Ramsey, M. S. (2002) *JGR-Planets*, 107, E8, 2156-2202.



**INSIGHTS INTO THE EARLY GEOLOGIC ERA OF MARS THROUGH ACID-SULFATE VAPOR WEATHERING OF PHYLLOSILICATES.** H.R. Edwards<sup>1</sup>, P.I. Craig<sup>2</sup>; <sup>1</sup>Department of Geosciences, Virginia Polytechnic Institute and State University, Blacksburg, VA 24060 (ehunter5@vt.edu); <sup>2</sup>Lunar and Planetary Institute, 3600 Bay Area Blvd, Houston, TX 77058 (craig@lpi.usra.edu).

**Introduction:** There are several hypotheses on how hydrated sulfate minerals formed on Mars, such as acidic weathering of phyllosilicates [1,2], and acidic weathering of basaltic materials [3,4,5]. For example, Altheide et al. researched acid leaching of phyllosilicate minerals [1], and Tosca et al. investigated acid-fog weathering of basaltic materials [3]. This study examines the formation of sulfuric minerals via acid-sulfate vapor weathering of phyllosilicates.

Phyllosilicates are mostly found in Noachian-aged [2, 6] terrains, a neutral-alkaline, wet period of Mars [1,7]. Phyllosilicates are also found near areas of Hesperian-aged hydrated sulfates [1,2,7]. Volcanic activity [8] and hydrothermal systems [9] during the transition from the Noachian to the Hesperian likely resulted in the formation of sulfate minerals currently present on the surface of Mars [3,7]. The close proximity of phyllosilicates to hydrated sulfates in select areas on Mars, such as Meridiani Planum [7] and Mawrth Vallis [10] (figure 1), gives clues to the geologic and aqueous history of the planet.

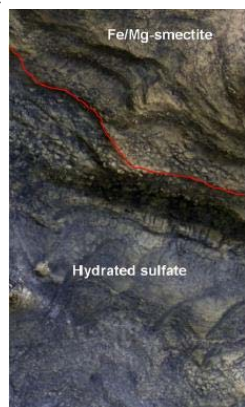


**Figure 1.** Hydrated minerals in Mawrth Vallis, Mars.

This study experimentally simulates the weathering process of volcanic acid-sulfate vapors on phyllosilicates. There are various types of phyllosilicates that have been found on Mars thanks to rovers and orbiters. Nontronite, an Fe-rich phyllosilicate, is the most abundant phyllosilicate on Mars [11]. However, there are Mg-rich [12] and Al-rich [1] phyllosilicates present as well. The release of sulfuric acid vapors from Hesperian volcanoes may be the cause of the correlations on Mars between these phyllosilicates and the hydrated sulfate minerals [1].

**Materials and Methods:** Four powdered phyllosilicates were obtained from the Clay Minerals Society

Source Clay Repository: Kaolinite (KGa-1)  $[\text{Al}_2(\text{Si}_2\text{O}_5)(\text{OH})_4]$ , nontronite (NAu-1)  $[\text{Na}_{0.3}\text{Fe}_2((\text{Si}, \text{Al})_4\text{O}_{10})(\text{OH})_2 \cdot n\text{H}_2\text{O}]$ , montmorillonite (STx-1)  $[(\text{Na}, \text{Ca})_{0.33}(\text{Al}, \text{Mg})_2(\text{Si}_4\text{O}_{10})(\text{OH})_2 \cdot n\text{H}_2\text{O}]$ , and saponite (SapCa-1)  $[\text{Ca}_{0.25}(\text{Mg}, \text{Fe})_3((\text{Si}, \text{Al})_4\text{O}_{10})(\text{OH})_2 \cdot n\text{H}_2\text{O}]$ . For experiments, 0.2g of each mineral was used. Teflon beads were placed on the bottom of a Teflon container, then approximately 2mL of concentrated  $\text{H}_2\text{SO}_4$  (sulfuric acid) was pipetted into the bottom of the container, underneath the beads. The samples were placed in platinum dishes, situated on top of the Teflon beads, in order to separate the samples from direct contact with  $\text{H}_2\text{SO}_4$ . The Teflon containers were then placed in Parr hydrothermal vessels and placed in an oven at the desired temperature. Four weeklong experiments were conducted on the unaltered phyllosilicate samples. Weathering processes took place at 50°C, 80°C, 100°C, and 125°C.

X-ray diffraction (XRD) patterns were taken of each sample to identify mineralogical changes. XRD analyses were conducted using a copper (Cu) source at 45kV and 40mA with a time per step of 10s, measuring samples from 4-80° 2θ. Scanning electron microscopy (SEM) with energy dispersive spectroscopy (EDS) were used to analyze the morphology of the samples. For SEM, samples were carbon coated prior to analyses to reduce conductivity and multiple images of different areas were taken.

**Results: Color.** Color alteration of the samples increased as the experimental temperature increased. The 50°C experiment did not reveal color alteration of any samples. Saponite-80°C was darker than the untreated samples. This was the only 80°C sample that had color alteration. Kaolinite, montmorillonite, and saponite were all slightly grayer following weathering at 100°C. Nontronite-100°C had no change in color following the experiment.

The 125°C samples had the greatest difference in color compared to the control samples and the other weathered samples. Every sample had extreme changes in the color. Kaolinite, montmorillonite, and saponite became much grayer. Nontronite became a darker shade of green. Montmorillonite-125°C revealed the greatest change in color of all samples, as the color of the exposed surface of the sample turned black (figure 2).





**Figure 2.** Left: Untreated montmorillonite. Right: montmorillonite-125°C on platinum dish.

**XRD.** The mineralogies for the untreated and 50° treated samples were very similar, with almost no variation between the two.

Mineralogies of the samples weathered at 80°C are comparable to the 50°C-treated samples and the untreated samples. There were no sulfuric minerals present in any of the samples.

Kaolinite-100°C did not reveal any sulfuric minerals that matched well with the sample. Montmorillonite-100°C contained hydrogen sulfide [ $\text{H}_2\text{S}$ ] (orthorhombic) and a sodium iron sulfate mineral [ $\text{Na}_6\text{Fe}(\text{SO}_4)_4$ ] (monoclinic). A potassium aluminum sulfate mineral [ $\text{KAl}(\text{SO}_4)_2$ ] (hexagonal) was detected in nontronite-100°C. Lanbeinite [ $\text{K}_2\text{Ca}_2(\text{SO}_4)_3$ ] (cubic), a potassium calcium sulfate mineral, was the sulfuric mineral present in saponite-100°C.

The 125°C samples revealed sulfuric minerals as well. Kaolinite-125°C contained an aluminum sulfate hydrate mineral [ $\text{Al}_2(\text{SO}_4)_3 \cdot 16\text{H}_2\text{O}$ ] (unknown crystal structure). Tamarugite [ $\text{NaAl}(\text{SO}_4)_2 \cdot 6\text{H}_2\text{O}$ ] (monoclinic), a sodium aluminum sulfate hydrate mineral, was present in montmorillonite-125°C. A sodium sulfate mineral [ $\text{Na}_2\text{S}_2\text{O}_3$ ] (cubic) was present in nontronite-125°C. Hexahydrate [ $\text{MgSO}_4 \cdot 6\text{H}_2\text{O}$ ] (monoclinic), a magnesium sulfate hydrate mineral, was analyzed in the mineralogy of saponite-125°C.

**SEM/EDS.** Analysis showed that the morphology and relative composition of the 50° treated samples was almost identical to the control samples. Analysis of the 125° treated samples revealed a sulfur composition among the relative elemental compositions, unlike the 50° treated samples. There were apparent structural differences in the samples, as monoclinic structures and orthorhombic structures were present. These two structures are associated with sulfuric minerals. Phyllosilicates have monoclinic structures, but not orthorhombic.

Due to time constraints and scheduling conflicts, SEM/EDS analyses of the 80 and 100 degrees samples were not conducted.

**Discussion/Conclusion: Color.** The sulfuric minerals present in the treated samples could be the reason for color alteration. However, the minerals found in XRD analyses of the phyllosilicates are colorless. Trace sulfuric minerals, trace elements [13], or contaminants could be the cause of the color alteration.

**XRD and SEM/EDS.** Due to samples treated at 50°C and 80°C not containing sulfuric minerals, or having changes in structure (for the 50°C), it can be interpreted that there was limited or no weathering present at these temperatures. It is plausible that the temperature and pressure conditions were not ideal for the  $\text{H}_2\text{SO}_4$  to become a vapor and cause weathering.

With the exception of kaolinite-100°C, all samples weathered at 100°C and 125°C revealed sulfuric minerals in their treated compositions from XRD analyses. XRD analyses of montmorillonite samples revealed development of new peaks (figure 3) as the samples became weathered at higher temperatures.

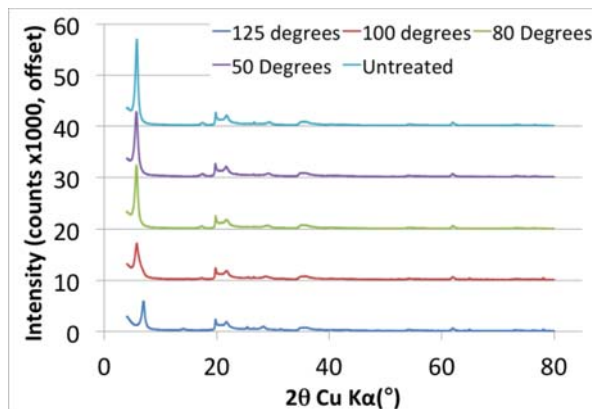


**Figure 3.** XRD peaks for unaltered montmorillonite and montmorillonite weathered at 50°C, 100°C, and 125°C

There were several hydrated sulfate minerals present in samples weathered at 100°C and 125°C. This is an important piece of evidence supporting acid-sulfate weathering of phyllosilicates considering data has shown that there are hydrated sulfate minerals adjacent to phyllosilicates on Mars [1, 2, 7].

Kaolinite-100°C did not reveal any sulfuric minerals from XRD analyses. It is possible that a sulfur-bearing phase was formed but at amounts below the detection limit. Additionally, kaolinite has been shown to be more resistant to liquid acid weathering [14] due to its 1:1 layered structure, as opposed to the other minerals' 2:1 structure.

Structural changes seen in SEM images for the 125° samples is further evidence for the formation of sulfates from sulfuric-acid vapor weathering of phyllosilicates. The typical monoclinic structures for phyllosilicates [15] were present, but there were also mono-

clinic structures that appeared to be very different than the ones of the untreated and 50°C (figure 4; pt.1). There were also orthorhombic structures that were only present in the 125° samples (figure 5; pt.1). These structures are typical for sulfate minerals [15]. They are also the crystal structures for a couple of the sulfuric minerals present in weathered samples. Having the orthorhombic structures present indicates that the odd monoclinic structures could be attributed to sulfuric minerals present in the sample.

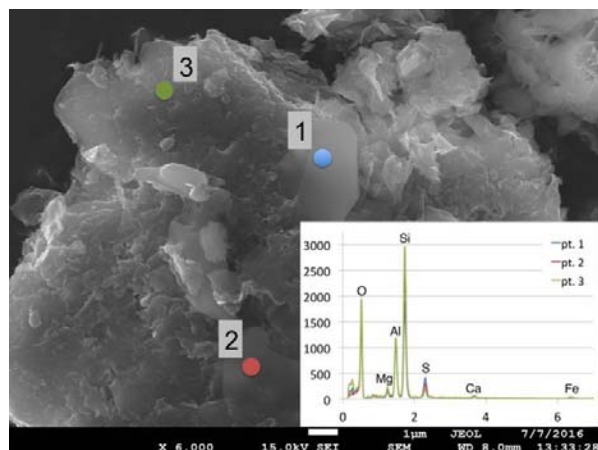


**Figure 4.** Differing monoclinic structures in treated montmorillonite-125°C SEM/EDS.

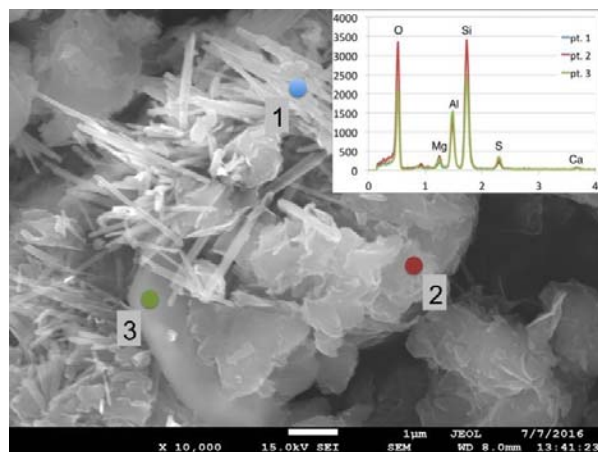


**Figure 5.** Orthorhombic structures seen in montmorillonite-125°C SEM/EDS.

Weathering at 50°C was not a high enough temperature to make the reaction kinetically favorable. However, there was clear evidence, visually and through instrumentation, that samples weathered at 80°C, 100°C, and 125°C underwent alteration.

As the temperature increased, weathering became greater. Montmorillonite was the most weathered element, and kaolinite was the least weathered. These

results are important for the interpretation of weathering events on early Mars.

**Implications for Mars:** The data collected in this survey provides evidence for the possible explanation for formation of Hesperian-aged sulfates adjacent to Noachian phyllosilicates, such as the rim of Endeavour Crater, Meridiani Planum [7]. The association of phyllosilicates and sulfates located adjacent to each other can also be seen at Mawrth Vallis [1]. Phyllosilicates form in the presence of water, and the formation of hydrous sulfate minerals from our experiments can be supporting evidence for the hypothesis that acidic volcanic vapors weathered nearby phyllosilicates, forming hydrous sulfate minerals.

Mars' sulfate minerals may not only be the result of the weathering of basalts, but also phyllosilicates, making the geologic history of Mars more diverse than previously thought. These results are important for understanding and replicating Mars' past geology, especially the link between the water-rich Noachian and acidic Hesperian.

**Acknowledgements:** The authors thank the Johnson Space Center and NASA for use of SEM and XRD as well as varying resources. USRA and the Lunar and Planetary Institute funded this study.

**References:** [1] Altheide et al. (2010) GCA 74, 6232-6248. [2] Craig et al. (2016) LPSC 2434. [3] Tosca et al. (2004) JGR 109, E05003. [4] McCollom et al. (2013) JGR 118, 577-614. [5] Golden et al. (2005) JGR 110, E12SO7. [6] Bibring et al. (2006) Science 312, 400-404. [7] Wray et al. (2009) GRL 36, L21201. [8] Hyneck et al. (2013) JGR 108, 2083-2104. [9] Marucci et al. (2013) JGR 118, 2213-2233. [10] Wray et al. (2010) Icarus 209, 416-421. [11] Andrieux et al. (2008) Workshop on Martian Phyllosilicates p.15 LPI Contribution No.1441, Lunar and Planetary Institute, Houston, TX [12] Wray et al. (2009) GRL 36, L21201. [13] Marucci et al. (2014) JGR 119, 679-703. [14] Craig et al. (2014) LPSC 1970. [15] Nesse (2000) Introduction to Mineralogy, Oxford University Press.

**LL-CHONDRITE NORTHWEST AFRICA 6813: SAMPLING AN IMPACT-CRATERED ASTEROID.**

L. Hoare<sup>1</sup>, M. Schmieder<sup>2,3</sup> and D. A. Kring<sup>2,3</sup>, <sup>1</sup>School of Earth Sciences, University of Bristol, Wills Memorial Building, Queens Road, Bristol, BS8 1RJ, United Kingdom ([lh13670@my.bristol.ac.uk](mailto:lh13670@my.bristol.ac.uk)) <sup>2</sup>Lunar and Planetary Institute, 3600 Bay Area Boulevard, Houston, TX 77058, <sup>3</sup>NASA-SSERVI.

**Introduction:** Impact cratering is one of the dominant geologic processes affecting asteroids. They result in shock-induced melting and the formation of impactites, including impact melt breccias. Meteoritic samples of these breccias possess petrologic and geochemical signatures that can be used to deduce the collisional evolution of the respective parent body, such as the timing of the event, shock metamorphic conditions during the impact, subsequent two-stage cooling, and an estimate of the size of the impact crater itself. In this study we analyzed the petrography and mineral chemistry of Northwest Africa (NWA) 6813 in order to elucidate its thermal and impact history. NWA 6813 was classified as an LL6 impact melt breccia [1], a group of ordinary chondrites whose impact lithologies and parent body evolution remain poorly constrained.

**Analytical Methods:** *Point Counts.* Point counting was conducted along lines with a separation of 300  $\mu\text{m}$  and a spacing of 100  $\mu\text{m}$  to determine the proportion of phases present in the thin section. This was done under reflected light using a LEICA optical microscope.

*Electron microprobe analyses.* A JEOL 8530F electron microprobe at the NASA-JSC was used to measure mineral compositions. All analyses were conducted using an accelerating voltage 15 kV. Mafic silicates were analysed using a 20 nA beam current and a 1  $\mu\text{m}$  beam diameter. Feldspathic components were analysed using a 10 nA beam current and a 2-4  $\mu\text{m}$  beam diameter. Metals and sulphides were analysed using a 30 nA beam current and a 1  $\mu\text{m}$  beam diameter (metals) and 3  $\mu\text{m}$  (sulphides). Some metal analyses were conducted along line scans with an analytical spacing of 2-4  $\mu\text{m}$ .

**Petrography and Geochemistry:** *General petrography.* Our thin section of NWA 6813 (sample DKLPI-174) is an impact-brecciated LL-chondrite with melt veins and pockets, and is characterised by two distinct lithotype domains: (i) a clast domain (CD), which is composed of 5 distinctive clasts, with two large clasts (1 and 5) 6.3×7.7 mm and 6.7×8.5 mm, respectively, exhibiting discrete textural contrasts and (ii) an optically dark, melt-bearing domain (DMB) that immediately surrounds smaller entrained chondritic clast fragments (Fig. 1). The dark domain contains regions of impact melt, consisting of veins and pockets of impact melt, some of which penetrate into the clast domain. A 4,296 point count of the thin section (~1.47 cm<sup>2</sup>) determined domain (i) represents ~68%, and domain (ii) ~32% of the sample. Clast 5 appears

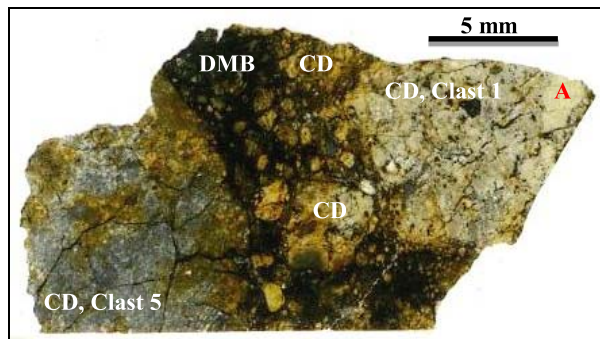


**Figure 1.** Thin section scan showing the clast domain (CD) and the dark, melt-bearing (DMB) domain.

darker than the rest of the clasts (Fig. 1). The sample is slightly weathered, with some metal and sulphide grains and shock veins showing signs of hematite alteration (<20% of grains), indicating weathering grade W1 [1,2]. Silicate and opaque shock veins cross-cut the clasts. Rare chromite and apatite (one apatite grain is intergrown with merrillite) are present, often in close proximity to metal, sulphide or oxide grains.

*Clast domain.* This domain is composed of ~83% silicates, ~1% oxides, ~2% metals, ~3% sulphides, and ~5% undivided metal/sulphides (<4  $\mu\text{m}$  in size) (normalised), which is consistent with the modal composition of other LL-chondrites [3]. The chondrule types present are predominantly porphyritic and barred olivine, as well as porphyritic and radial pyroxene, with occasional porphyritic olivine-pyroxene. The average chondrule diameter is ~570  $\mu\text{m}$ , which is comparable to other LL-chondrites [4]. Interstitial hypidiomorphic olivine crystals locally measure up to ~300  $\mu\text{m}$  in size, with pyroxene usually  $\leq 200$   $\mu\text{m}$  in size. Many chondrules possess a feldspathic mesostasis. There are rare interstitial feldspar grains in the matrix up to ~200  $\mu\text{m}$ . Mono- and polyminerallc metal, sulphide (troilite), and oxide grains up to ~400  $\mu\text{m}$  are present. The dominant particle/aggregate size fraction of metals and sulphides is  $\leq 1.0$ -16.0  $\mu\text{m}$ , with a few metal and sulphide particles in the range of 60-1000  $\mu\text{m}$  (Fig. 2). Clast 1 contains a large (2.1×2.9 mm) olivine-pyroxene object (A in Fig. 1), with an orthopyroxene oikocryst poikilolitically enclosing smaller euhedral olivine grains. The object locally shows a 'barred' texture and well-defined contacts with the surrounding clast.

*Dark, melt-bearing domain.* This domain is 84% silicates, 4% oxides, 2% metals, 1% sulphides, and 9% undivided metal/sulphide (<4  $\mu\text{m}$  in size) (normalised).



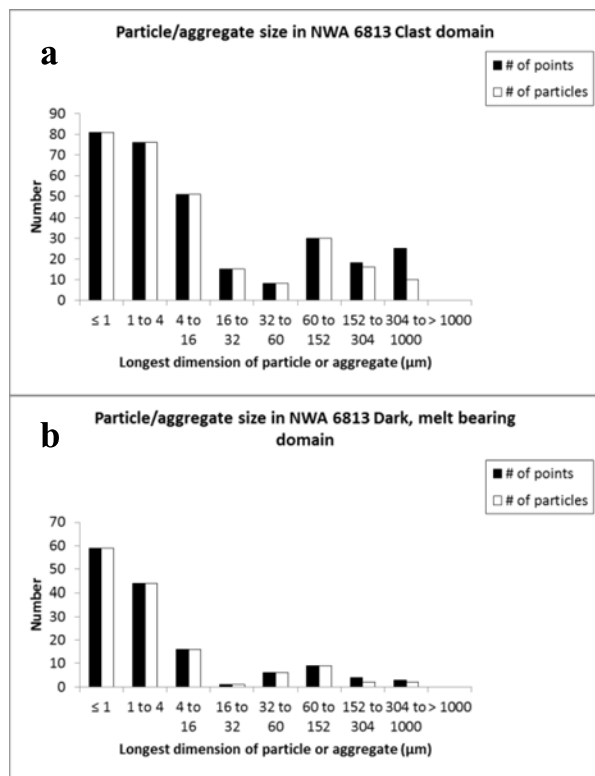


**Figure 2.** Histograms of metal and sulphide particle size distribution in (a) clast domain and (b) dark, melt-bearing domain.

The domain is cataclastic with numerous entrained fragments of rounded to irregular-shaped light-coloured clast material suspended in an optically dark aphanitic 'matrix' (Fig. 1). The optically dark areas are due to presence of abundant small metal/sulphide particles. Chondrules are barred olivine, porphyritic olivine and/or pyroxene, and radial pyroxene. Individual relic subhedral to anhedral grains of olivine and pyroxene are present within the optically dark regions, typically ranging from ~15 to ~300  $\mu\text{m}$  in size. Localised pockets or veins of impact melt are also present with characteristic orbicular metal-sulphide particles and partially melted clast fragments, both typically ~5–30  $\mu\text{m}$  in size, all contained within an aphanitic, cryptocrystalline, melt matrix composed of olivine, pyroxene, and minor sulfide and chromite (Fig. 3). The dominant particle/aggregate size distribution of metals and sulphides is  $\leq 1.0$ – $4.0$   $\mu\text{m}$ , with a few particles in the range of 16–152  $\mu\text{m}$  and rare particles  $>152$   $\mu\text{m}$  (Fig. 2).

**Geochemistry.** Olivine is  $\text{Fa}_{25.2-30.4}$  ( $n=56$ ), however, the majority of compositions fall in the range of  $\text{Fa}_{28-29}$ , which is consistent with other LL-chondrites [5]. Pyroxene compositions exhibit a wider degree of variability. Some pyroxene crystals are zoned, with low-Ca cores surrounded by high-Ca rims of pigeonite, and rarely augite. High-Ca pyroxene ( $>5\%$  Wo) is rare, and

is  $\text{Wo}_{5-43}$   $\text{En}_{47-75}$   $\text{Fs}_{10-21}$  ( $n=6$ ). Low-Ca pyroxene is  $\text{Wo}_{1-4}$   $\text{En}_{69-89}$   $\text{Fs}_{11-30}$  ( $n=65$ ). The composition of olivine and low-Ca pyroxene in the clast domain is similar to those in the dark, melt bearing domain.  $\text{FeO/MnO}$  for olivine, low-Ca pyroxene, and high-Ca pyroxene is 57.2–58.0, 33.9–36.7, and 30.2–32.2, respectively, all of which are comparable to ratios obtained from other LL chondrites [6,7]. Feldspar compositions are  $\text{Ab}_{29.5-88.4}$   $\text{Or}_{1.68-71.8}$   $\text{An}_{1.7-28.1}$  ( $n=77$ ), however, the majority were highly sodic ( $\text{Ab}>75$ ). Metal particles are either kamacite or taenite; some particles are zoned with kamacite cores and taenite rims. Ni concentrations in taenite range from ~23.9 to ~38.6 wt%. Kamacite contains Co concentrations with an average of ~2.8 wt%, which falls within the typical range for LL-chondrites [8]. Sulphide is dominantly troilite (~35–36 wt% S), with minor sulfide richer in Fe (~42–50 wt%). Pyroxene within the unusual olivine-pyroxene object in clast 1 (A in Fig. 1) shows a distinct trend with  $\text{TiO}_2$  and CaO increasing with respect to  $\text{Al}_2\text{O}_3$  (wt%), distinguishing it from the clast and dark melt-bearing domains.

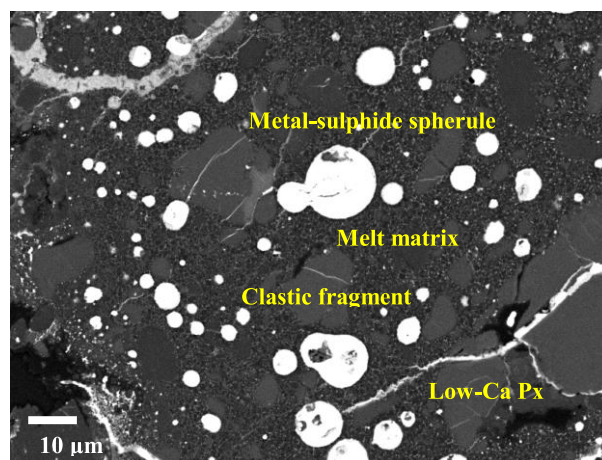


**Figure 3.** SEM image of an impact melt pocket in the dark melt-bearing domain, with metal-sulphide droplets and entrained relic mineral clasts (mostly olivine) in a cryptocrystalline melt matrix. Cross-cutting shock veins and fractures are also present.

**Metamorphism: Thermal Metamorphism.** Olivine in clasts 1–4 is relatively homogeneous, whereas pyroxene shows slightly more variation. Low-Ca pyroxene is predominantly orthorhombic, which indicates a high petrologic type (5–6) [5]. Chondrule rim sharpness is well-defined to readily delineated, and feldspar predominantly occurs as microcrystalline aggregates  $\leq 50$   $\mu\text{m}$  in size, which indicates type 4–5 [5]. Turbid igneous glass is present in some chondrules, and the matrix is a mixture of transparent microcrystalline and recrystallised material, which suggests type 4–5 [5]. The maximum Ni content of Fe,Ni-metal, kamacite

and taenite, is >20 wt%, and the average Ni content of sulphide minerals is <0.5 wt%, which suggests type 4 and above [5]. However, there is evidence indicating clast 5 might represent a higher petrologic type. Its chondrules are predominantly poorly defined, and feldspar usually forms interstitial grains  $\geq 50 \mu\text{m}$  in size, with some up to  $300 \mu\text{m}$ . The texture of the matrix in clast 5 is recrystallized and may represent type 5-6 [5]. The grade of thermal metamorphism is not uniform across the melt breccia sample, which is dominantly composed of LL5 clasts with a subordinate LL6 component (clast 5).

**Shock Metamorphism.** Undulatory extinction, planar fractures, and mosaicism are all present within 20 randomly selected olivine grains in the two largest clasts (1 and 5), and indicate shock stage S5-6, although it seems to lack ringwoodite and significant maskelynite. These features, together with the presence of ubiquitous veins and pockets of impact melt (Fig. 3), suggest a shock stage of S6, i.e. shock pressures of  $\sim 45\text{--}90 \text{ GPa}$  and a post-shock temperature increase of  $600\text{--}1750 \text{ }^\circ\text{C}$  [9], according to the original classification of Stöffler et al. [9], which is consistent with the initial shock stage ascribed to NWA 6813 [1].

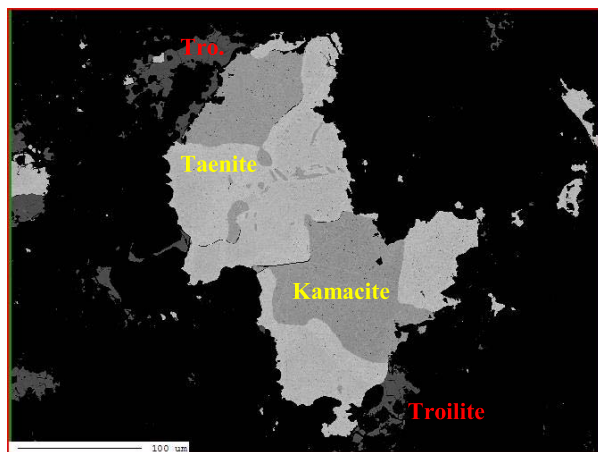


**Figure 4.** A typical metal particle in the clast domain with sharply contrasting taenite and kamacite zones locally surrounded by troilite. BSE image. Scale bar is  $100 \mu\text{m}$ .

**Metallography:** The metal and sulphide grains in this sample possess a slight bimodal size distribution (Fig. 2). Textural variation is apparent, ranging from distinctly zoned particles with pure kamacite and taenite zones (Fig. 4) to rare plessite, with some unusually large plessite grains ( $\sim 30 \mu\text{m}$ ). Small metal-sulphide spheres are present in the impact melt, some of which contain small ( $\sim 2\text{--}5 \mu\text{m}$ ) metal cells. The width of these metal cells was tentatively used to calculate a stage 1 cooling rate for the superheated melt, using the

method of Scott [10]. Cell widths of  $2\text{--}5 \mu\text{m}$  suggest a tentative stage 1 cooling rate of  $\sim 5,000\text{--}70,000 \text{ }^\circ\text{C/sec}$ . No meaningful stage 2 cooling rate could be calculated because of the high Ni concentration ( $>20\text{--}50 \text{ wt\%}$ ) in the metal [11], characteristic of LL-chondrites [12]; however, cooling was presumably (very) fast. High Ni in troilite ( $>0.1 \text{ wt\% el.}$ ) and the small size of metal-sulphide melt orbs also indicate fast cooling.

**Discussion:** The heterogeneity in petrologic type is possibly the result of an impact event on an LL-chondrite asteroid. Another explanation could be impact-induced melting and mixing of a previously impact-brecciated target, possibly a pre-existing clastic breccia containing both LL5 and LL6 clasts. However, the lack of large melt-entrained clasts makes this scenario less likely. The distinct trends in  $\text{TiO}_2$  and CaO in the unusual olivine-pyroxene object in clast 1 could possibly be the result of igneous processes and, thus, that object could be an anchondritic fragment, potentially of LL-derivation, based on Fa# and FeO/MnO values of olivine.

**Conclusions:** Our sample represents an LL5 melt-bearing impact breccia, probably formed within the structural floor of an impact crater. The NWA 6813 parent asteroid experienced thermal metamorphism to an LL5/6 stage, followed by S6 shock metamorphism. The heterogeneous petrologic types of clasts could be the result of impact-related brecciation and/or partial impact-melting and mixing of various lithologies that formed the asteroid target at the time of impact. Prior to the impact event, LL5/6 material and some igneous material had possibly been present at or near the asteroid surface. Following the impact event, the melt-bearing impact breccia underwent rapid two-stage cooling.

**References:** [1] Rubin A. E. (2012) The Meteoritical Bulletin, #99. *Meteoritics & Planetary Sci.*, 47(11), 38. [2] Wlotzka F. (1993) *Meteoritics*, 28, 460-460. [3] Weisberg M. K. et al., (2006) in *Meteorites and the Early Solar System II*, 19-52. [4] Rubin A. E. (2000) *Earth Sci. Rev.* 50, 3-72. [5] Van Schmus W. R. and Wood J. A. (1967) *Geochim. Cosmochim. Acta*, 31, 747-76. [6] Rubin A. E. and Swindle T. D. (2011) *Meteoritics & Planetary Sci.*, 46, 587-600. [7] Rubin A. E. (2000) *Geochim. Cosmochim. Acta*, 66, 3327-3337. [8] Afiattalab F. and Wasson J. T. (1980) *Geochim. Cosmochim. Acta*, 44, 431-446. [9] Stöffler D. et al., (1991) *Geochim. Cosmochim. Acta*, 55, 3845-3867. [10] Scott E. R. D. (1982) *Geochim. Cosmochim. Acta*, 46, 813-832. [11] Jarosewich E. (1990) *Meteoritics*, 25, 323-337. [12] Willis. J and Goldstein J. I. (1981) *Proc. Lunar Planet. Sci.*, 12B, 1135-1143.

**PETROLOGY OF IGNEOUS CLASTS IN HOWARDITE METEORITES.** Z. V. Hodges<sup>1</sup> and D. W. Mittlefehldt<sup>2</sup>, <sup>1</sup>Department of Earth Sciences, Durham University, Science Labs, Durham, DH1 3LE (z.v.hodges@durham.ac.uk) <sup>2</sup>Astromaterials Research Office, NASA Johnson Space Center, Houston, TX 77058.

**Introduction:** The howardite, eucrite and diogenite (HED) clan of meteorites are widely considered to originate from asteroid 4 Vesta [1]. Basaltic eucrites are fine to medium grained rocks composed of pigeonite (low-Ca pyroxene) and plagioclase formed in flows and in shallow to deep intrusive bodies [2]. Cumulate eucrites are medium to coarse grained gabbros [2]. Diogenites are coarse-grained cumulate ultramafic rocks formed at depth in the crust; most diogenites are orthopyroxenites, but harzburgites [3] and dunites [4] have also been documented. Howardites are polymict breccias dominantly composed of lithic clasts and mineral fragments of eucritic and diogenitic origin, as a result of impact fragmentation and mixing of the crust of the eucrite parent body.

Two main petrogenetic models exist to explain the formation of HED lithologies and thus the thermal history of the parent body itself: partial melting [5] versus a magma ocean (extensive melting; the current consensus view) [6-7]. A global magmatic stage would allow silicate material to be well mixed, destroying any initial heterogeneity that may have been present.

Measurements show that most eucrites and diogenites have uniform  $\Delta^{17}\text{O}$  ( $\Delta^{17}\text{O}$  is the deviation of O isotopic ratios from the terrestrial mass-dependent fractionation line), this is considered to be a result of homogenization through a global magmatic stage of at least 50% melting of the parent body [8]. Some mafic achondrites have small isotopic anomalies however (e.g. Pasamonte), and these are interpreted to be derived from parent asteroids other than Vesta [9].

The Fe/Mn ratio of mafic phases in planetary basalts can be diagnostic of different source bodies as this ratio is little-affected by igneous processes, so long as the oxygen fugacity is buffered [10]. Most HEDs have similar Fe/Mn ratios in pyroxene [10], though some meteorites have been found to have pyroxene Fe/Mn ratios outside of the normal range of 31-33 commonly found in eucrites (e.g. Ibitira [11]).

Mafic clasts in howardites are likely all from the eucrite parent asteroid. The alternative is that ejecta from multiple differentiated parent bodies landed on Vesta, mixed in with the regolith and eventually became lithified. Based on Occam's razor, the former, simpler case with fewer assumptions is more likely to be true.

Here, pyroxene Fe/Mn ratios in mafic clasts in howardites will be tested to determine whether the parent asteroid is uniform. Uniformity would suggest that the parent asteroid was subject to homogenization

prior to the formation of the HED lithologies, likely through an extensive melting phase. Whereas, distinct differences may point towards heterogeneity of the parent body, or the need for multiple parent asteroids.

**Samples and Methods:** Igneous clasts in two howardites, EET 87503 and DOM 10837, were examined and compared to a reference unbrecciated basaltic eucrite, EET 87520. Clast textures were characterized using optical microscopy and scanning electron microscope (SEM) back-scattered electron (BSE) imaging.

Pyroxene and plagioclase from individual clasts within each thin section were analysed using electron microprobe analysis using the Cameca SX100 and JEOL 8530F electron microprobes at NASA Johnson Space Center. Analytical conditions for plagioclase were 15 kV potential, 20 nA sample current and a 3  $\mu\text{m}$  spot size. Conditions for pyroxenes were 20 kV, 40 nA, 1  $\mu\text{m}$  spot and counting times of 120 and 40 seconds for Mn and Fe respectively. Such conditions for pyroxene analysis allow for a better than 2%  $1\sigma$  standard deviation precision on the mean for Fe/Mn ratio for low-Ca pyroxenes – these conditions were sufficient to resolve differences in Ibitira pyroxenes from those of basaltic eucrites [11].

A third sample, LAR 12326, was also examined using optical microscopy and SEM imaging. However, it appeared that this meteorite might be a polymict eucrite, and so no further analyses were taken.

Pyroxene compositions are compared using Fe/Mn. Most eucrites show evidence of thermal metamorphism, which is inferred from the presence of augite exsolution lamellae within low-Ca pigeonite hosts and lack of Fe/Mg zoning [12]. Fe and Mn partition differently in pigeonite and augite, as such only low-Ca pyroxenes are used for comparisons here.

Normality tests were conducted to establish the distribution of the data for each clast. Statistical techniques, such as the Student's t-test, were used to compare Fe/Mn ratio means for low-Ca pyroxenes in individual clasts in both howardites to those in the reference basaltic eucrite, EET 87520.

**Petrology and Mineral Compositions:** Howardite EET 87503 has an overall fragmental brecciated texture containing abundant lithic clasts within a clastic matrix composed of single crystal fragments (Fig. 1). The matrix is composed of varying grain sizes of pigeonite, augite, plagioclase, orthopyroxene, metal and silica. Lithic clasts show a variety of textures from igneous subophitic basaltic clasts with unequilibrated, highly zoned pyroxenes, to highly metamorphosed



clasts with granoblastic texture and equilibrated pyroxenes. Equilibrated and unequilibrated are used qualitatively here to describe levels of equilibration, be that high or low [12]. Impact melt clasts and chondritic clasts are also evident.

Howardite DOM 10837 has much more variety in its matrix than EET 87503. The majority is a fine grained igneous matrix breccia with subophitic texture composed of plagioclase and pyroxene that contains larger, rounded to sub-rounded mineral grains of dominantly pigeonite and plagioclase. Whereas, part is a fragmental matrix breccia of individual mineral grains and fragments more similar to that in EET 87503. Examples of lithic clasts studied include those with equilibrated pyroxenes, that lack zoning, and sub-ophitic igneous texture. Some clasts show small pockets of mesostasis of silica and opaque phases, such as metals. Impact melt clasts are also present.

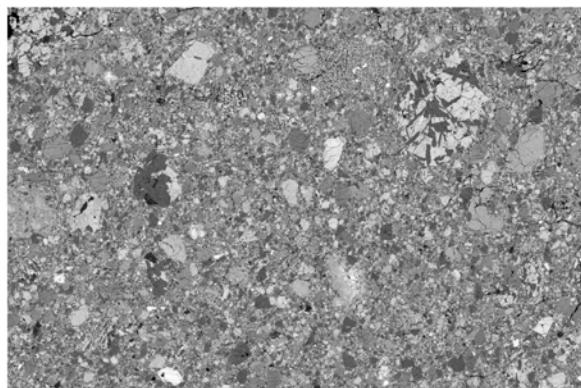


Figure 1: BSE image of EET 87503. Lithic and mineral clasts are visible within the fragmental matrix. Image is 12 mm across.

Example pyroxene quadrilaterals show the great variability in pyroxene compositions in EET 87503. The highly metamorphosed clast 5 shows clear distinction between pigeonite and augite compositions as a result of equilibration (Fig. 2a). In contrast, clast 6 contains pyroxenes that are highly unequilibrated and display igneous zoning (Fig. 2b). All clasts analysed in DOM 10837 have pyroxenes displaying equilibration, none show evidence of zoning and some are more Fe-rich than the reference eucrites EET 87520 and Sioux County (e.g. clast 3, Fig. 2c).

For clasts within EET 87503, the overall average plagioclase composition ranges from  $An_{86-92}$ . Internal clast compositions show a variety of ranges with some being very narrow, e.g. clast 5  $An_{88.5-89.0}$ , and some much wider, e.g. clast 10  $An_{81.0-92.4}$ . The average plagioclase composition in DOM 10837 ranges  $An_{78-88}$  and, similarly to in EET 87503, individual clasts show varied ranges.

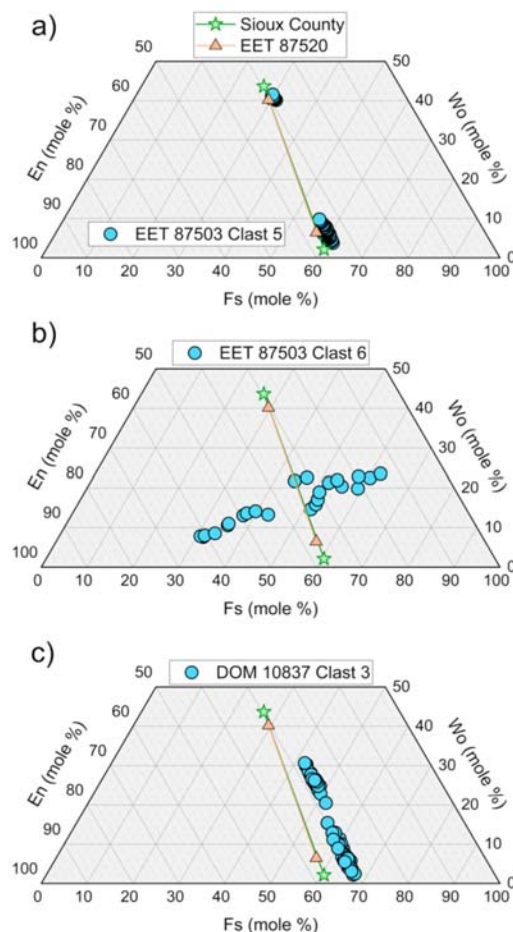


Figure 2: Example pyroxene quadrilaterals for individual clasts in each howardite compared to eucrites Sioux County and EET 87520.

**Discussion:** Anomalous petrographical features, such as vesicles (e.g. Ibitira [11]), cannot be adequately characterized in the clasts because of their small size. As such, the mineral compositions of individual clasts provide a more solid basis for comparison.

Statistical tests on mafic clasts from EET 87503 and DOM 10837 (16 and 4 respectively), compared to that of the reference eucrite EET 87520, reveal that there are robust differences in Fe/Mn ratios at the 99% confidence level (Fig. 3). Such differences are much smaller than those found for anomalous eucrite-type achondrites such as QUE 94484, EET 87542 and Ibitira [11,13].

As Fe/Mn ratios can be used to fingerprint basalt source bodies [10], these variations could be interpreted as evidence for either compositional heterogeneity in the HED parent body or separate parent bodies. The former leads to the question as to whether the HED parent body actually underwent extensive differentiation through extensive melting (magma ocean), as this would in theory erase any traces of initial heterogeneity.

ty [8]. Alternatively, though the majority of basaltic eucrites have so far demonstrated homogeneous oxygen isotopes, indicating homogenization of the parent body [8], there are examples of mafic achondrites with distinctive isotopic and petrologic characteristics. These might indeed point towards an origin on parent bodies distinct from that of the HED clan, as is the case for Ibitira [11,15]. The variations observed here however, are much smaller than those of anomalous achondrites postulated to originate from a distinct parent body. Future work testing clasts from these howardites for anomalies in oxygen isotopes will help to determine both the possibility of a magma ocean and the need for more than one parent body.

On the other hand, should our assumption that the HED meteorites are derived from a single parent body hold, the small differences in Fe/Mn ratios of mafic clasts point towards small intrinsic variations within the parent body crust. Variations that could still arise within pyroxenes on a single parent body that underwent a global magma ocean stage.

A simple model of the effect on Fe/Mn and Fe/Mg ratios with varying molar Fe is plotted in Figure 3. The variation in clast Fe/Mn is consistent with either the addition or removal of Fe through redox processes, or through simple igneous fractionation processes.

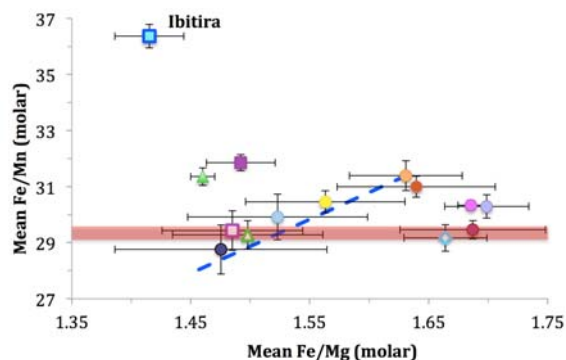


Figure 3: Mean Fe/Mn vs. mean Fe/Mg for individual clasts within EET 87503. Filled symbols are significantly different from the reference eucrite Fe/Mn (shown as red band). The effect of varying molar Fe is represented by the blue dashed line.

Redox processes could, for example, involve late stage reduction of FeO, perhaps as a result of increasing  $f_{S_2}$  and sulphur saturation with cooling and crystallization [13]. Subsolidus reduction of FeO should form Fe metal, silica and magnesian pyroxene with low Fe/Mn. If the reducing agent was S, the mesostasis would likely be rich in a sulphide, such as troilite [13,14]. Evidence of pockets of mesostasis of silica and metal is sparse in clasts of EET 87503, though there is evidence of small portions of mesostasis in clasts of DOM 10837. As mentioned previously, this

scarcity may be a result of the small scale of clasts analysed here (a few hundred microns) relative to cm-sized thin sections of mafic achondrites.

Igneous fractionation results in the crystallizing pyroxenes to have lower Fe/Mg and Fe/Mn than the melt [5]. The apparent trend of basaltic clasts in Fe/Mn and Fe/Mg (Fig. 3) may therefore simply be a result of increasing igneous fractionation.

The relatively small differences in Fe/Mn ratios in mafic clasts in EET 87503 and DOM 10837 compared to those in anomalous mafic achondrites raises the question as to whether the differences determined here are due to preserved heterogeneity on the parent body or simple igneous processes, such as crystal fractionation.

**Summary:** Our results show statistically sound variations in low-Ca pyroxene Fe/Mn of individual clasts in howardites, EET 87503 and DOM 10837. While this variation in Fe/Mn ratio could be a result of a heterogeneous parent body that did not undergo extensive differentiation or multiple parent bodies, we think that what can be concluded from these results is that Fe/Mn ratios can vary slightly even on a homogeneous, differentiated body. These small statistical differences then actually have geological significance regarding the detailed history of individual magma pulses. These results provide important constraints on using pyroxene Fe/Mn in interpreting the petrology of basaltic eucrites.

**Acknowledgements:** We thank Kent Ross, Eve Berger, Loan Le and Anne Peslier for their assistance in labwork. This project was funded through the NASA Emerging Worlds Program.

**References:** [1] McSween Jr. H. Y. et al. (2013) *Meteoritics & Planet. Sci.*, 48, 2090-2104. [2] Mittlefehldt D. W. (2015) *Chemie der Erde*, 75, 155-183. [3] Beck A. W. and McSween Jr. H. Y. (2010) *Meteoritics & Planet. Sci.*, 45, 850-872. [4] Beck A. W. et al. (2011) *Meteoritics & Planet. Sci.*, 46, 1133-1151. [5] Stolper E. (1977) *Geochim. Cosmochim. Acta*, 41, 587-611. [6] Righter K. and Drake M. J. (1997) *Meteoritics & Planet. Sci.*, 32, 929-944. [7] Ruzicka A. et al. (1997) *Meteoritics & Planet. Sci.*, 32, 825-840. [8] Greenwood R. C. et al. (2005) *Nature*, 435, 916-918. [9] Scott E. R. D. et al. (2009) *Geochim. Cosmochim. Acta*, 73, 5835-5853. [10] Papike J. J. et al. (2003) *Am. Min.*, 8, 469-472. [11] Mittlefehldt D. W. (2005) *Meteoritics & Planet. Sci.*, 40, 665-677. [12] Takeda H. and Graham A. L. (1991) *Meteoritics*, 26, 129-134. [13] Mittlefehldt D. W. et al. (2016) *LPS XLVII*, Abstract #1240. [14] Mayne R. G. et al. (2009) *Geochim. Cosmochim. Acta*, 73, 794-819. [15] Wiechert U. H. et al. (2004) *Earth Planet. Sci. Lett.*, 211, 373-382.



**CORRELATING SWIRLS WITH PARTICLE TRACKING SIMULATIONS AT LUNAR MAGNETIC ANOMALIES IN SOUTH POLE-AITKEN BASIN AND MARE CRISIUM.** R. Karimova<sup>1</sup>, G. Y. Kramer<sup>2</sup>, E. M. Harnett<sup>3</sup>, <sup>1</sup>Department of Physics and Earth Sciences, Jacobs University Bremen, Campus Ring 1, 28759 Bremen, Germany, <sup>2</sup>Lunar and Planetary Institute, 3600 Bay Area Blvd, Houston, TX 77058, <sup>3</sup>Department of Earth and Space Sciences, University of Washington, 4000 15<sup>th</sup> Avenue NE, Seattle, WA 98195-1310.

**Introduction:** Lunar swirls are high albedo curvilinear features that do not follow local topography, and appear optically immature compared to their surroundings. They are located at the lunar magnetic anomalies, however not all anomalies have identified swirls [1] [2]. One of the theories that explain the origin of the swirls suggests that swirls are areas of retarded surface weathering due to shielding from the solar wind ions by the anomalous magnetic fields [1].

The area for the study presented here covered the South Pole- Aitken basin (SPA) and Mare Crisium. Swirls were mapped using several multispectral datasets. The maps were correlated with particle tracking simulations to test the solar wind deflection hypothesis on the SPA anomaly. For Crisium they were used to constrain the areas for swirl search and explore possible reasons for the lack of apparent swirls in the Mare Crisium magnetic anomaly.

*Space weathering:* The Moon is constantly bombarded by solar wind particles and micrometeorites due to the lack of an atmosphere and a global magnetic field. The physical and chemical changes in the regolith due to these influences are termed space weathering. Formation of nanophase iron (npFe<sup>0</sup>) is one of the processes that results from space weathering. The optical properties of npFe<sup>0</sup> are responsible for the changes in reflectance of regolith that has been exposed to space weathering, which includes decrease in overall reflectance, increase in spectral slope and reduced absorption band depths [3].

*Magnetic anomalies and solar wind deflection model:* The crustal magnetic anomalies on the Moon have been first detected by Apollo 15 and 16 [4] and subsequently mapped by multiple other spacecraft. Observations by Lunar Prospector, Nozomi, SELENE/Kaguya, Chandrayaan-1, and Chang'E-2 have shown that solar wind particles could be deflected by the mini-magnetospheres formed at these magnetic anomalies [5].

The efficiency of the magnetic field to deflect solar wind depends on its strength and coherence. The coherence of the field defines how fast the magnetic field directions change over distance. A more dipole-like field would change less often with distance, and would be stronger at deflecting incoming solar wind. Determining the coherence requires analyzing the spherical harmonic expansion of the field or by studying its 3D structure [5].

Swirls only *appear* less optically mature than the surrounding areas. [6] have shown that the material on the

swirls is the same age as in the surrounding darker optically mature terrain. The finding suggests that fresh material deposited by crater ejecta is weathered faster on off-swirl areas than on swirls, supporting the solar wind deflection model. Off-swirl locations experience higher rate of weathering caused by an increased flux of solar wind particles impacting on their surface, due to deflection of the particles away from the swirl areas [6].

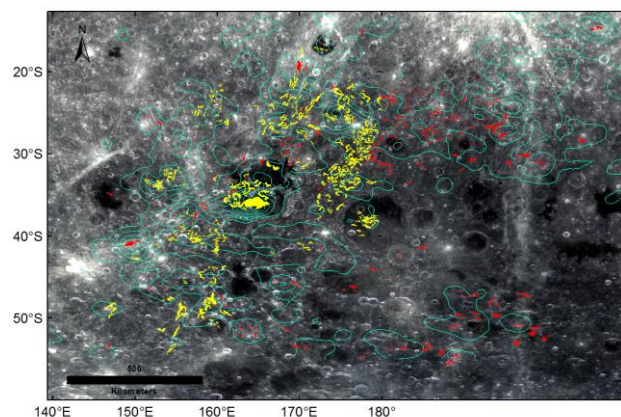


Figure 1: WAC normalized reflectance map of SPA basin. Swirls mapped by [7] are shown in yellow. Magnetic field lines are in green.

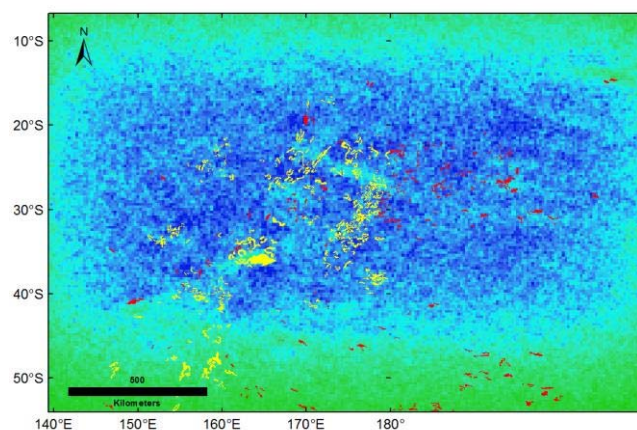


Figure 2: Proton density map for SPA. High values shown in blue and low values in green.

**Methods:** The datasets used for identifying swirls included Lunar Reconnaissance Orbiter Wide Angle Camera (LRO WAC) 643 nm normalized reflectance map ([http://wms.lroc.asu.edu/lroc/view\\_rdr/WAC\\_GLOBAL](http://wms.lroc.asu.edu/lroc/view_rdr/WAC_GLOBAL)), slope map derived from the LRO Global Lunar Digital

terrain model (WAC\_GLD100; [http://wms.lroc.asu.edu/lroc/view\\_rdr/WAC\\_GLD100](http://wms.lroc.asu.edu/lroc/view_rdr/WAC_GLD100)), and a false color band ratio map derived from LRO WAC reflectance map (415 nm was displayed as red, 321/415 nm ratio as green, and 260/415 nm as blue) [7]. Combined use of these datasets proved helpful in identifying the swirls in the SPA basin: overlaying the normalized reflectance WAC map with 70% transparent slope map helped eliminate the topography effects on the reflectance, and the false color map displayed the swirls in bright magenta/red with a good contrast from the surrounding material. Additionally, optical maturity (OMAT),  $\text{TiO}_2$ , and FeO abundance maps were derived from Kaguya (SELENE) Multiband Imager (MI) mosaics [8] [11] [12], to improve the identification of the swirls, and compare with the signatures of the swirls on different parameter maps.

After being tested on the SPA region, the same datasets were used to search for swirls in Mare Crisium anomaly in combination with the particle tracking simulation results. The density and flux maps from particle tracking proved useful in constraining areas where swirls could be found in a previous study on the Northwest of Apollo magnetic anomaly [5] [13].

**Particle tracking:** Simulated anomalous magnetic field used for the particle tracking simulations was obtained from [http://www.planetary-mag.net/moon\\_interface.html](http://www.planetary-mag.net/moon_interface.html) [9]. The model used for particle tracking simulation is described in [10]. 400,000 non-interacting protons were launched on the magnetic anomaly of Mare Crisium, and 800,000 for SPA due to the larger extent of the area. Protons were chosen for the simulations because they are considered the primary reducing agents for the formation of  $\text{npFe}^0$  [5] [6]. They were tracked till they impacted on the surface or left the simulation area due to deflection by the field. Density and flux maps generated from the simulation results were normalized to nominal solar wind densities at 1 AU of 5 particles/ $\text{cm}^3$ , and compared to the swirl maps.

**Results and discussion: SPA:** South Pole-Aitken is the largest lunar basin located on the far side of the Moon. The study area was therefore extensive, about  $3.7 \times 10^6 \text{ km}^2$ , and included some areas such as Mare Ingenii and NW of Apollo, where swirls have been mapped previously [6] [7].

In addition to the well-known large scale and complex swirls in Mare Ingenii, and a large density of smaller swirls on highland material between the Birkeland and Leeuwenhoek craters (yellow in Figure 1), new swirls (red in Figure 1) have been mapped extending to the north-east of Leeuwenhoek, and to the east to Orlov crater. This study found another smaller concentration further south around Bose crater. Individual swirls were found scattered across the overall study area (Fig. 1). Mapping the SPA swirls allowed us to cross check their signatures in all the datasets and derived parameter maps.

The SPA magnetic anomaly consists of multiple smaller anomalies within the basin. Particle tracking re-

sults showed several locations with significant proton deflection in agreement with the mini-anomalies. Swirl locations coincided with these sites of low particle fluxes and densities very well (Fig. 2), which indicates that they were shielded from the solar wind and are less weathered as a result. The swirls on the southernmost part of SPA and some swirls on the periphery were outside of the proton beam in the simulation which can be seen on Fig. 2 as the highest particle concentration area in blue. Whether or not these swirls are located in density cavities has to be confirmed by extending the particle tracking simulation region. It is worth noting that as in the previous study by [5], particle tracking could predict approximate swirl locations and not individual swirls, due to the coarseness of the model resolution, which is limited by the available magnetic field strength measurements on the Moon.

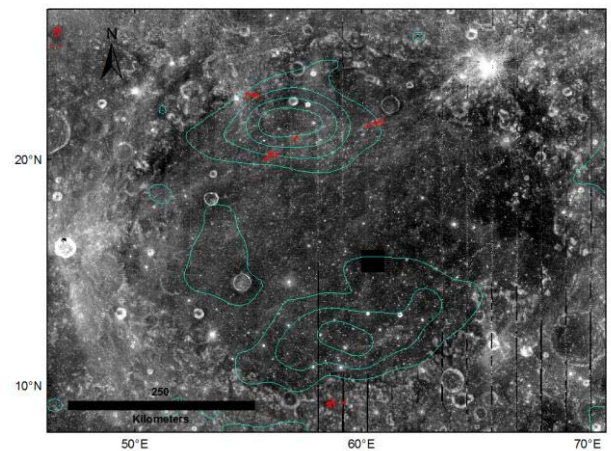


Figure 3: OMAT map of Mare Crisium. Magnetic field contours shown in green and potential swirls in red

**Crisium:** Mare Crisium is one of the medium strength magnetic anomalies ( $\sim 23 \text{ nT}$ ) [2], and is notable for the lack of identified swirls, which was the reason for selecting it as our study area. The anomaly region contains two locations where the field strengths reach local maximums (Fig. 3). Particle tracking showed deflection of particles only on the stronger northeastern part (Fig. 4). It is however less efficient than the deflections on SPA, where some of the strong anomalies had areas of zero proton density.

We attempted to identify possibly faint swirls in the low particle density sites as well as on the entire study area by co-registering multiple images. A candidate site with several faint small swirls in the range of about 2-6 km in length, was found on the northwestern rim of the mare, at the lower particle density region (Fig. 3, 4). The swirls were best visible in the OMAT map overlain by the semi-transparent inverted slope map (Fig. 3). They seem to have the usual swirl signature in all the images used in this study, such as independence from the local topography and a high OMAT value (i.e. they are immature). However, all the signals are very faint, which does not allow one to conclusively define these features as swirls. It



is also difficult to outline their extent since they are located on bright highland material.

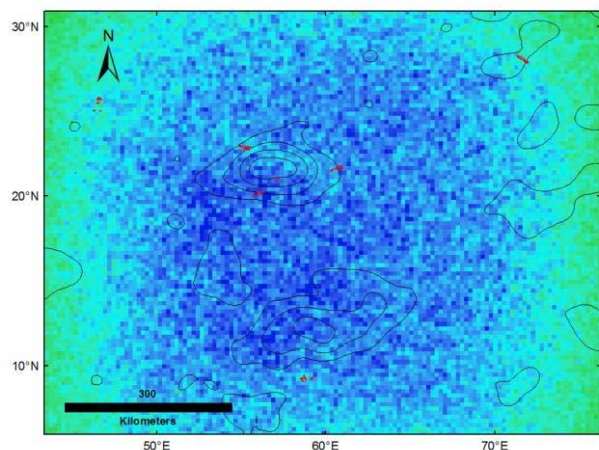


Figure 4: Proton density map of Mare Crisium. High values are shown in dark blue, low values in green.

Even if these small features were identified as swirls, it is still unusual that significantly more distinct and complex swirls are not found in Crisium, but are present in other magnetic anomalies that have similar field strength (e.g. Mare Marginis). Particle tracking results could explain why we do not observe swirls. They have shown that the Crisium anomaly deflects significantly fewer particles and only in a small region compared to the strong anomalies in SPA. The reason for this could be the structure of the magnetic field on Mare Crisium.

We generated slices of the magnetic field components ( $B_x$ ,  $B_y$ ,  $B_z$ ) at different altitudes for the purpose of inferring the coherence of the Crisium anomaly. The  $B_z$  component slice at the surface (Fig. 5) shows that the northern anomaly has a strong  $-B_z$  and a weak  $+B_z$  components, while the southern part has a very weak  $-B_z$ . As a result, the weak  $+B_z$  in the north combines with the strong  $+B_z$  in the south creating a mostly radial magnetic field over the mare. The weak deflection observed at the northwestern rim of the mare occurs at the transition between the positive and strong negative  $B_z$ , where the field is tangential to the surface, and would be able to deflect incoming protons. We plan to further investigate the 3D magnetic field lines to get a better idea of the field structure. One also has to take into account the limitations of the source magnetic field data: its coarse resolution could be averaging out finer scale features of the field, making it appear more coherent than it actually is [5].

**Conclusion:** Mapping swirls in South Pole-Aitken basin showed that using the false color band ratio image in combination with the slope map, OMAT, FeO and TiO<sub>2</sub> helped to identify a number of new swirls. SPA swirls coincide with low particle flux and density cavities, supporting the solar wind deflection model. On the other hand, we were not able to find definitive evidence of swirls in the controversial Crisium anomaly. Particle simulation results showed only a weak deflection of pro-

tons around the northwestern rim of the mare, where faint, small candidate swirls have been mapped. The lack of strong particle deflection here can be explained by the 3D structure of the magnetic anomaly. Examination of the  $B_z$  component slices suggested a radial magnetic field over the mare, with a small tangential part at the site where a weak deflection was observed. More investigation into the magnetic field structure is planned to confirm these structure inferences. Additionally, finer scale surface magnetic field measurements could provide useful insights for investigating the Mare Crisium anomaly.

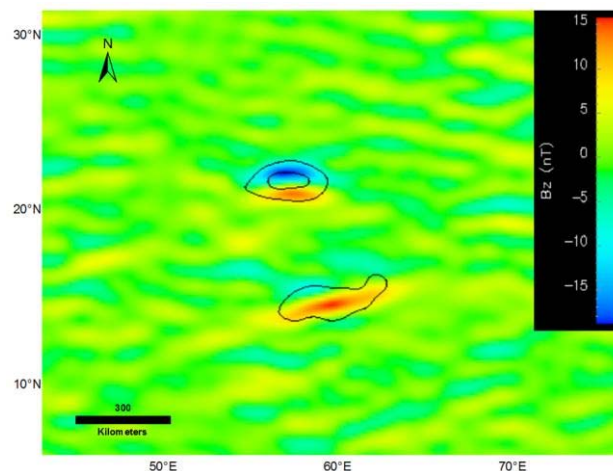


Figure 5:  $B_z$  component slice at the surface at Mare Crisium.

**References:** [1] Hood and Williams (1989) *PLPSC* 19. [2] Blewett et al., (2011) *JGR* 116.E2. [3] Denevi et al., (2014) *JGR* 119.5 976-997. [5] Harnett et al., (2016) *arXiv preprint arXiv:1605.05778*. [6] Kramer et al., (2011) *JGR* 116.E4. [7] Denevi et al., (2016) *Icarus* 273: 53-67. [8] Otake et al., (2012) *PLPSC* 43. [9] Purucker and Nicholas (2010) *JGR* 115.E12. [10] Harnett and Winglee (2000) *JGR* 105.A11 24397-21007. [11] Lemelin et al., (2016) *LPSC* 47. [12] Lemelin et al., (2015) *JGR*, 120, 869–887, doi:10.1002/2014JE004778. [13] Tai Udovicic (2015) *31<sup>st</sup> Annual LPI Summer Intern Conference* 31-33.

**ANALYZING NORTH AMERICAN METEORITE FALLS TO DEVELOP A MASS PREDICTION METHOD USING NOAA RADAR REFLECTIVITY DATA.** C. E. Laird<sup>1</sup>, M. D. Fries<sup>2</sup> <sup>1</sup>Dept. of Earth, Environmental, and Planetary Sciences, Case Western Reserve University, Cleveland, OH 44016 (cel76@case.edu) <sup>2</sup>Astromaterials Research and Exploration Science, NASA Johnson Space Center, Houston, TX 77058.

**Introduction:** During recent years, there have been many advances in the use of sensory equipment, such as weather RADAR, seismometers, and all-sky cameras, to aid and expedite the recovery of meteorites. These techniques allow new insights in the physics of meteorite fall dynamics and fragmentation during “dark flight”, or the period of time between the end of the meteor’s luminous flight and the concluding impact on the ground. Understanding dark flight dynamics allows us to rapidly analyze the characteristics of new meteorite falls, making it possible to increase the frequency and total mass of scientifically important freshly-fallen meteorites available to the scientific community. The specific interest of this paper is to explore the quantification of meteorite fall mass while a meteor is still in dark flight using reflectivity data as recorded and distributed by National Oceanic and Atmospheric Administration (NOAA) Next Generation RADAR (NEXRAD) stations. This study analyzed eleven official and one unofficial meteorite falls in the United States and Canada (listed in Table 1) to achieve this purpose.

RADAR reflectivity data is accessible on the NOAA website, and can be viewed using NOAA’s Weather and Climate Toolkit. Reflectivity values (dBz) are the product of RADAR pulses interacting with an object. The object absorbs, scatters, and reflects certain fractions of the pulse power depending on the physical characteristics of the material and the distance from the initial RADAR source. The portion of reflected RADAR waves returned to the RADAR receptor are converted to power received ( $P_R$ ).  $P_R$  is then used to calculate the reflectivity ( $z$ ) of that return according to the RADAR equation:  $P_R = \frac{\pi P_E G^2 \theta \phi h |K|^2 L z}{1024 \ln(2) \lambda^2 r^2}$  (eq. 1) [1]. For the purposes of this study, the equation listed above was flipped and simplified to  $z = \frac{P_R}{c |K|^2}$  (eq. 2), with  $c$  as a constant representing the accumulation of the fundamental constants of NEXRAD stations and values precalculated by the NEXRAD system, and  $K^2$  expressing the target’s material-dependent dielectric properties. The source of this value is the equation  $|K|^2 = \left| \frac{\epsilon - 1}{\epsilon + 2} \right|^2$  (eq. 3) [1],  $\epsilon$  being the target’s dielectric constant. For weather system analysis, meteorological scientists have developed the equation:  $z = n D^6$  (eq 4) [1] where  $z$  is total

reflectivity,  $n$  is the number of particles in a RADAR sweep, and  $D$  is the expected diameter of the particles. Note that meteorological calculations used to express RADAR reflectivity are based on reflection from water. For analysis of meteorite falls, we much convert these values using the dielectric constants of meteorite materials

It is important to note that the range of altitudes of a meteor fall monitored on RADAR, between approximately 0.5km and 20km, is within the meteor’s dark flight. With knowledge concerning RADAR quantification and the skills necessary to identify meteor falls on weather RADAR as described in [2], this study seeks to develop a method to estimate the total mass of meteoritic material present during the dark flight section of a meteor fall from reflectivity values and fall specific data such as terminus height, entry angle and local wind velocity.

**Methods:**

*Empirical Approach.* By utilizing NOAA’s Weather and Climate Toolkit software and NEXRAD RADAR data, meteorite fall activity was recognized and then quantified in terms of the absolute value of total reflectivity per radar sweep by summing the reflectivity value associated with each meteorite pixel (Figure 1). The resulting totals were graphically analyzed to discover any possible trends between reflectivity and recoverable meteorite mass.

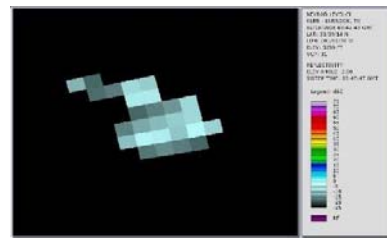


**Figure 1:** Mount Blanco Meteorite Fall as seen on RADAR. Blue/gray pixels visually show reflectivity from falling meteorites.

*Theoretical Approach.* The reflectivity totals found in the previous section provided the starting point for a more in-depth theoretical analysis of the selected meteorite falls. As a result of the NEXRAD system’s calibration to precipitation (water and ice), it was necessary to correct the initial reflectivity values for meteoritic material before proceeding. Using two versions of equation 2:

$$z_{\text{water}} = \frac{P_R}{c |K_{\text{water}}|^2} \quad \& \quad z_{\text{meteorite}} = \frac{P_R}{c |K_{\text{meteorite}}|^2},$$

the corrective value ( $x$ ) was determined to be  $x =$

$\frac{|K_{\text{water}}|^2}{|K_{\text{meteorite}}|^2}$  (eq. 5). NEXRAD uses K-squared value of 0.93, and the K-squared values for meteoritic material were calculated using equation eq. 3 and the dielectric constants for L, LL, H type meteorites [3] and dry asphalt (as an analog for carbonaceous meteorites) [4]. These values were used in equation 4 to produce meteorite type specific corrective x-values, which were in turn applied to the z values from the Empirical Approach to convert them to the appropriate  $z_{\text{meteorite}}$  values. The result was a set of reflectivity values appropriate for falling meteorites as opposed to rain. The meteorite reflectivity totals for z and  $z_m$  are displayed in Table 1.

For further analysis, we extended the process used by meteorological scientists to measure rainfall by modifying equation 4 to fit the specifications of meteorites. This resulted in the equation:  $n = (0.2742) \frac{z_m \rho^2}{m^2}$  (eq. 6) where n= number of meteorites,  $\rho$ = meteorite density (dependant on classification), m= mass of meteorites belonging in the RADAR sweep, and the constant accounts for the assumed geometry of the meteorites. To simplify the equation, it was assumed that meteorites are spherical and of uniform density.

To acquire the necessary values for equation 6, extensive analysis of each fall was required. Specifically, to find the mass of meteorite pieces belonging in the scanned portion of the fall, many fall details and theories of projectile motion were used to calculate mass distribution based on dark flight modeling. Dr. Fries's dark flight model, JÖRMUNGANDR (acronym: Just because JÖRMUNGANDR) mathematically predicted the mass of the pieces present at the each scan time and altitude. Fall details consisted of fireball terminus altitude, terminus time (seconds accuracy), initial velocity, initial angle below the horizontal, initial direction, meteorite density [5], scan times (with seconds accuracy), scan altitude, local wind velocity, atmospheric density and atmospheric temperature. A technical bug in the NOAA freeware was found to misrepresent the accuracy of sweep times by up 50 seconds and necessitated the manual correction of the scan time data. A correction procedure developed by Dr. Rob Matson solved this problem. For multiple falls with terminus times undocumented by literature or video, IRIS seismic data was utilized to calculate the time in which the meteor's sonic boom occurred. It was assumed that the sonic boom occurred at the same time as fireball illumination ceased and was located directly above the fall site. The Pythagorean Theorem was used to calculate the distance of the direct path from the sonic boom to the seismic station, and the speed of sound through the

atmosphere was calculated from weather balloon data. From these values, it was possible to back-calculate the time of the fireball terminus. For terminus altitude, initial velocity and initial angle, averages from an accumulation of literature values [6,7] were calculated to be 22km, 4100 m/s, and 40.4 degrees, respectively, and used where directly measured values were unavailable.

Each sweep's JÖRMUNGANDR determined mass, known density (dependent on meteorite type) and totaled  $z_m$  value were used with equation 6 to calculate the number of meteorites of that mass present in the scan.

The resulting data for number of meteorites per RADAR sweep was plotted versus the corresponding mass values to produce histograms of RADAR observable mass distribution. Two power law fitting methods were used to fit the histograms and estimate the quantity of masses missed by RADAR in between scan revolutions according to the mass range of the fall. The first method utilized plotting software to strictly fit the experimental data for the smaller falls (with  $z_m$  values under 1500 dBZ) with the best fit power law function. The second fitting method was modeled after the known Moravka meteorite fall's in-flight mass distribution to best fit the experimental data with a set exponent (b) value of -1.45 [8]. This method was used for falls above  $\sum z_m > 1500$  dBZ, as empirical results indicate improved fidelity of the calculation with recovered mass values. Following estimation, recovery efficiency was calculated and analyzed.

**Results: Empirical Approach.** Figure 2 shows the results of the initial study of the relationship between the total sum of uncorrected reflectivity (z) and total recovered mass. Park Forest has been removed from the plot as an outlier because of the anomalously high recovery. Also, the 02 Jun 2016 unnamed AZ fall is not included because recovered mass data is currently unavailable. This plot resulted in a linear fit equation of  $y = 3.6952x - 512.28$  ( $R^2 = 0.599$ ), which can be used as a rough estimate of how much mass can be recovered from a fall based on reflectivity data alone.

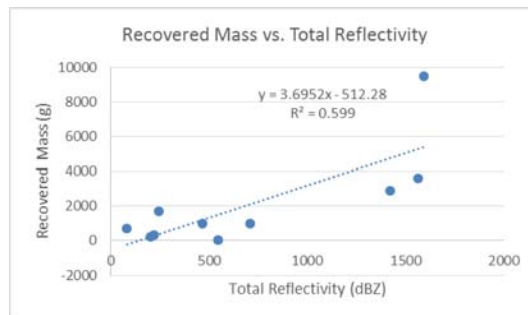


**Figure 2:** Plot of Recovered Mass vs. Total Reflectivity seen on RADAR. Each point represents one fall.



Fall	Meteorite Type <sup>a</sup>	Recovered Mass (g) <sup>a</sup>	Reflectivity Z (dBZ)	Corrected Reflectivity Z <sub>m</sub> (dBZ)	Fit Type	Total Mass Estimate (g)	Recovery Efficiency (%)
Ash Creek (2009)	L6	9500	1592.5	3992.0	Moravka	11,394.20	83.4
<i>Mifflin (2010)</i>	<i>L5</i>	<i>3580</i>	<i>1565.5</i>	<i>3924.3</i>	<i>n/a</i>	<i>n/a</i>	<i>n/a</i>
Battle Mountain (2012)	L6	2900	1422	3564.6	Moravka	30,940.30	9.4
Osceola (2016)	L6	991	711	1774.8	Moravka	18,366.90	5.4
Park Forest (2003)	L5	18000	670	1679.5	Moravka	28,068.90	64.1
Mount Blanco (2016)	L5	36.2	546	1368.7	Strict	9,832.00	0.4
Sutter's Mill (2012)	C	993	467	1206.4	Strict	23,457.50	4.2
<i>Indian Butte (1998)</i>	<i>H5</i>	<i>1721</i>	<i>246</i>	<i>608.1</i>	<i>n/a</i>	<i>n/a</i>	<i>n/a</i>
Lorton (2010)	L6	330	220	551.5	Strict	10,979.20	3.0
Grimsby (2009)	H5	215	204.5	504.5	Strict	21,915.10	1.0
Creston (2015)	L6	688	82.5	206.8	Strict	3,081.90	22.3
<i>AZ Unnamed (2016)</i>	<i>LL?</i>	<i>n/a</i>	<i>82</i>	<i>250.9</i>	<i>Strict</i>	<i>20,023.20</i>	<i>n/a</i>

**Table 1:** Summary of Known and Estimated Values for the Studied Meteorite Falls

<sup>a</sup>Classification by the Meteoritical Society, published in the Meteoritical Society Bulletin.

**Theoretical Approach.** Of the twelve meteorite falls used in this study, full analysis was possible for nine. Two falls, Mifflin and Indian Butte, resulted in unreasonable fit functions and were excluded. Also, it is impossible at the current time to analyze the AZ fall for efficiency without recovered mass data. Analysis included summation of reflectivity, meteorite specific adjustment of the reflectivity sum, power law fitting, estimation of the total mass of meteoritic material, and assessment of recovery efficiency for each fall (Table 1).

The power law fitting process was two-steps, starting with a literature value meteorite mass distribution curve fit function of  $y=ax^b$ , where  $y$  is number of meteorites and  $x$  is mass. The first, Strict Fit, procedure was initially attempted for all of the falls. However, this method lead to wildly erroneous estimates for high-mass falls (determined as “large” by  $z_m$  data). For this reason, strict fitting was only utilized for falls below an empirically derived  $z_m = 1500$  dBZ cutoff. The

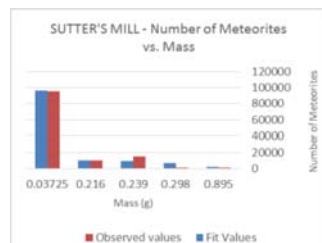


**Figure 3:** Fit Accuracy Comparison Histogram

results of strict fitting are shown in the bottom portion of Table 1. For each fall, a comparative graph showing the accuracy of the fit to the observable data was created (Figure 3). The best fit curve was applied to a histogram of mass value bins to estimate the unobserved masses, filling out the curve and enabling total mass estimation (Figure 4).

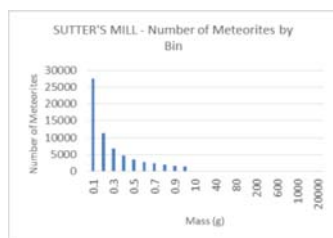


**Figure 4:** Best Fit Curve Histogram for Estimation

For the larger meteorite falls studied, a power law fit was used from the well-characterized mass distribution of a large-sized meteorite fall, Moravka. This produced reasonable estimations for larger falls, but anomalously

low estimations for smaller falls. We believe this represents a fundamental variation in the fragmentation behavior of “large meteoroids. The results for this method can be seen in top portion of Table 1.

Following estimation, the recovery efficiency was calculated. The results are shown in Table 1's last column and graphed against Total Mass Estimate in Figure 5.

**Discussion:** The method presented in this study is a fundamentally new tool to aid fresh meteorite recovery. As shown on the bottom row of Table 1, with access to reflectivity data it is possible to develop a generalized estimate of fall mass before any meteorites are recovered. These models and estimates provide a glimpse into the mysterious nature of meteor dark flight by describing and quantifying in-flight mass distribution. The numerical products of this study also provide new insight into meteorite recovery. The three falls showing high (above 10%) recovery efficiency in Table 1 and Figure 6 were located on search-friendly terrain with high search participation, suggesting correlation between ideal search conditions and high recovery rate. Under typical conditions, it can be expected that less than ten percent of a meteorite fall is recovered for scientific study.

It is the hope of this study that this method is utilized and improved upon to supplement the amount of freshly fallen meteorites available to the scientific community in the future.

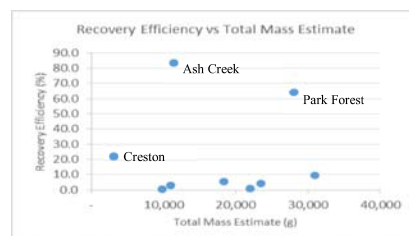


**Figure 6:** Scatter Plot Showing the Distribution of Recovery Efficiency vs Fall Size.

**References:** [1] Skow, K. (2013) *National Weather Service*. [2] Fries M. et al. (2013) *LPSC XLIV*, 2935. [3] Heggy E. et al. (2012) *Icarus*, 221, 925-939. [4] Shang J., Umana J. (1999) *Journal of Infrastructure Systems*, 5, 135-142. [5] Britt D., Consolmagno S. (2003) *Meteoritics & Planetary Sci.*, 38, 1161-1180. [6] Gritsevich M. (2008) *Solar System Research*, 42, 372-390. [7] Brown P. et al. (2013) *Meteoritics & Planetary Sci.*, 48, 270-288. [8] Borovicka J., Kalenda P. (2003) *Meteoritics & Planetary Sci.*, 38, 1023-1043.



**REASSESSING THE SIZE AND MORPHOLOGY OF THE HAUGHTON IMPACT STRUCTURE.** C. W. Patterson<sup>1</sup> and V. L. Sharpton<sup>2</sup>, <sup>1</sup>Department of Earth Science, Carleton University, 1125 Colonel By Drive, Ottawa, ON, Canada K1S 5B6 (calderpatterson@email.carleton.ca), <sup>2</sup>Lunar and Planetary Institute, 3600 Bay Area Blvd, Houston, TX 77058.

**Introduction:** The Haughton impact structure (HIS) is an Eocene-aged complex crater formed ~39 Ma [1] in the western portion of Devon Island, Nunavut, Canada. While much of the original near-surface signature of the crater has been removed, a striking assemblage of geological and geophysical features are retained within its distinctive, well-documented target stratigraphy. A wealth of field data, including a near-radial seismic line [2], gravity measurements [3], and detailed geological mapping [4,5], offers a unique opportunity to understand the product of hypervelocity impact into soft, volatile-rich targets. Previous analyses [2,3,6,7] provide a general morphological model wherein the original crater was ~24 km diameter (10-12 km diameter transient crater) and complex, but with no central peak structure. The overarching goal of this study is to use modern geospatial information system analytics to test and refine this model.

**Target:** The HIS target consists of ~1900 m of westward dipping (>4°) Ordovician to Silurian carbonates, overlying a crystalline basement [6]. An extensive breccia unit covers the crater centre. However, isolated outcrops outside of this area suggest that the breccia and ejecta originally covered a significantly larger area [4]. Large outcrops of the Haughton Formation, referred to as “lake deposits”, were deposited shortly after the formation of the impact structure and are also preserved in the centre of the crater [7].

**Methods:** Available spatial information (geologic mapping, topography, and gravity data [3]) were analysed both separately and integrally. Geologic mapping [4,5] was digitized in ArcGIS (Fig. 3) to integrate it with other digital geospatial information. A fixed crater centre was constrained (at 75°22'41"N, 89°40'46"W) based on its geometric positioning and a point with the lowest Bouguer anomaly (~-6 mgal).

Conventional cross-sections of HIS proved to be inadequate because erosion has acted non-uniformly on the crater surface morphology. We therefore devised a new method that analyzes radially oriented, wedge-shaped areas (Fig. 1) in order to identify relationships between key structural and lithological features that constrain the original surface shape of the crater. The map area was divided into eight individual wedges (comprising 4 diametric couplets).

The regional gravity field has a distinct southward sloping trend decreasing ~0.141 mgal/km to the south-southwest, which obscured the influence of the crater's gravity anomaly. The regional trend was subtracted from the original data to generate a corrected raster image (Fig. 2). A histogram of the corrected map shows a unimodal distribution with a standard deviation ( $\sigma$ ) of ~2.5 mgal around the regional mean. A surface slope tool was used to describe the rate of change of the gravity anomaly on the pixel scale. 3 classes were defined based on relative rates of change, which are defined as low, moderate and high.

**Observations:** The central region of the crater is marked by a topographic low that becomes indistinct as distance from the crater centre increases. The greatest density of faults and boundaries occurs between ~5 and 8 km from the centre, although crater fill deposits obscure the innermost extent of this zone. In the western portion of HIS, target rocks (Lower Allen Bay Fm) emerge from beneath the crater fill at radial distances of ~6 to 7.5 km and (presumably) *in situ* shattercones

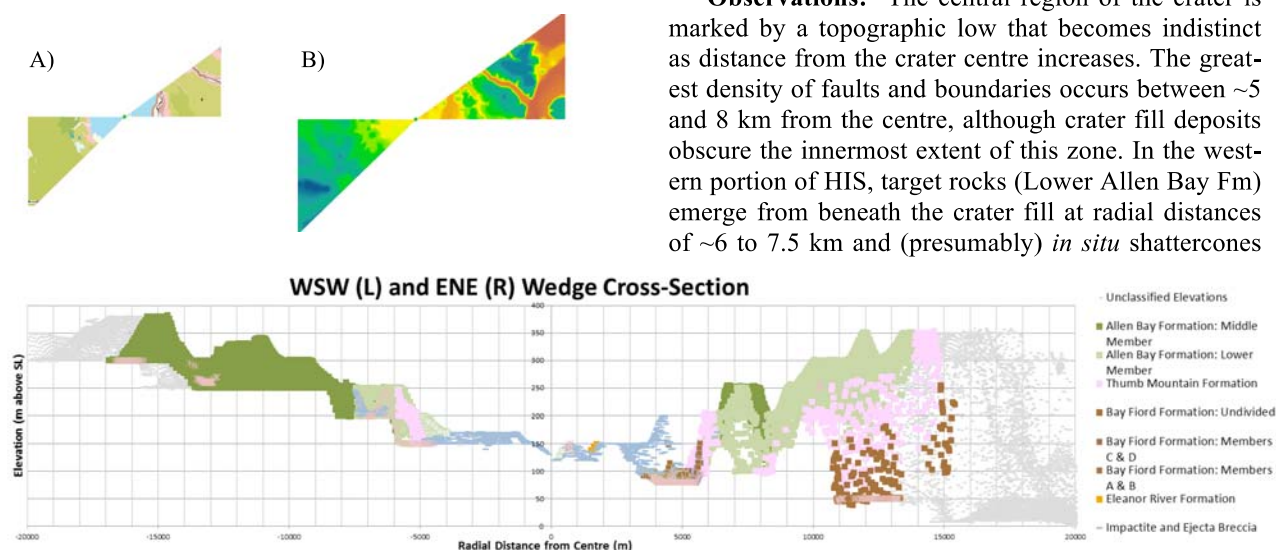


Figure 1. Wedge cross-section example (bottom) with accompanying overviews (top left) of the geological map (A) and topography (B) from the associated sample area.

have been reported to the south located  $\sim 7.4$  km from centre. Beyond this, boundaries and faults were mapped at distances as great as  $\sim 14$  km [4,5]. Interestingly, canyons in the outer reaches of the crater commonly appear to adhere to circumferential and radial controls and in some cases are observed to follow mapped boundaries and faults. These features were traced and have been identified at radii greater than 14 km.

In all of the wedge cross-sections, a distinct topographic low is observed outwards to  $\sim 1$  km. This area is completely occupied by the breccia unit and some outcrops of the lake sediments but have been modified by more recent fluvial and glacial sedimentation. Some cross-sections display peaks of deeper target rocks (Eleanor River Formation) distinctly rising above both the remaining lake deposits and breccia unit with radial extents from  $\sim 1$  to 1.5 km outwards to  $\sim 2$  to 4 km. A well-defined bowl shape with a consistent radius of  $\sim 5$  to 5.5 km and a depth of  $\sim 50$  to 75 m is observed in all cross-sections. Extensive outcrops of the lake deposits in the north and west are plastered onto the walls of this bowl structure. Outward and upward-stepping terraces, each  $\sim 2$  to 3 km wide with vertical offsets of  $\sim 30$  to 50 m, are observed beyond the inner depression (Fig. 1). In some cases, they are observed extending as far as  $\sim 14$  km from the centre, up to the regional plateau, between  $\sim 350$  and 400 m above sea level.

HIS exhibits a nearly circular gravity anomaly, but only to an outer radial boundary located at  $\sim 7.5$  km (Fig. 2). The inner most observed gravity anomaly equal to the regional mean is at a radial distance of  $\sim 8$  km. Beyond a radius of  $\sim 7.5$  to 8.0 km, the gravity anomaly has no apparent geometric configuration that can be associated with HIS. Instead, there is a chaotic zone with an anomaly between  $-2.5$  and  $2.5$  mgal, which makes it statistically insignificant as it does not exceed  $\pm 1 \sigma$ . The central crater anomaly has a magnitude below  $-3 \sigma$ ,  $< -7.5$  mgal to a radius of  $\sim 1$  to 2 km and  $< -10.0$  mgal to a radius of  $\sim 0.5$  to 1 km.

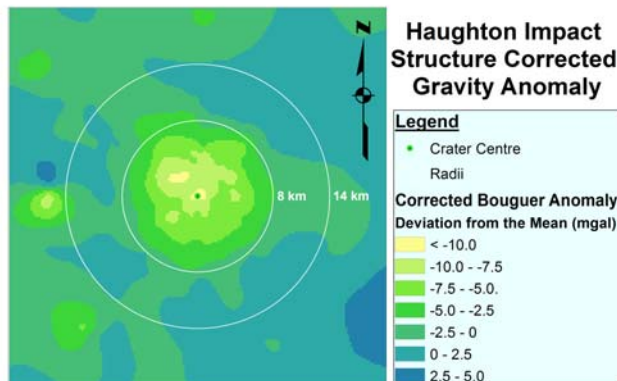


Figure 2. Raster image of the corrected HIS regional gravity anomaly [6].

Between radii of  $\sim 7$  and 8.5 km, there is a nearly continuous ring of moderate to high gravitational rates of change. A second, more poorly defined ring of moderate to high rates of change is between  $\sim 4$  and 6 km. Between  $\sim 2$  and 4 km there is an area of low to moderate rates of change. At the centre of the crater is a zone with a radius of 1 to 1.5 km where there is a very distinct high rate of change of the gravity anomaly, which corresponds in both size and shape with the previously described inner zone of low gravity ( $-7.5$  mgal to  $< -10.0$  mgal).

**Discussion:** Based on the structural and gravity anomaly observations outlined above, there are several distinct regions that can be interpreted. These regions exhibit unique gravity signatures and structural features; the bands with high rates of gravitational change are interpreted to be transitional boundaries between these zones.

The central gravity anomaly low ( $< -10.0$  mgal with a radius of  $\sim 0.5$  to 1.0 km) and the topographic low, occupied by the brecciated unit, are indicative of a central area of deep excavation. The high rate of gravitational change and a strong magnetic anomaly with a radius of 1.5 km [3] supports this theory and helps to constrain the radius of deep excavation to be between  $\sim 1.0$  and 1.5 km [8].

The outcropping peaks of uplifted material identified between  $\sim 1.0$  and 4.0 km from the crater centre are interpreted to be a central structure that is best described as a poorly formed proto-peak ring. The edge of the bowl-shaped structure beyond these peaks with a radius of  $\sim 5.0$  to 5.5 km correlates with a transitional zone between 4.0 and 6.0 km. Extensive outcrops of the lake beds in the north and west are plastered onto the walls of this bowl structure, suggesting that the bowl and the central peaks have undergone little erosion in contrast to the rest of the crater [7]. The central bowl structure is interpreted to be the area most greatly affected by the late-stage subsidence of the crater centre.

Due to the regional dip of the underlying target material the Lower Allen Bay Fm (ABL) should be buried under several hundred metres of the Middle Allen Bay Fm (ABM) in the western portion of the mapped area. This and a preserved contact with an outcrop of the breccia unit suggests ABL was not only uplifted from greater depths, but was also within the area of effect (AOE) of the excavated crater so that the ejecta breccia was deposited on top of it and not ABM, which should otherwise overly it. The shattercones to the South of the crater centre are interpreted to be in-place and associated with the interior of the transient crater. These two pieces of evidence suggest that the transient crater has a radius greater than 7.4 km. The outer most transitional gravity ring correlates with the outer edge of the circular gravity anomaly as well as the outer-most evi-

dence for the transient crater rim and the extent of the greatest fault density, therefore the transient crater is interpreted to have a radius of ~8.0 km.

Beyond the transient crater, the gravity anomaly has no apparent geometric configuration or statistical significance. Previous studies [6] have suggested that an apparent crater rim can be defined in radial profiles, which only sample a very finite portion of the crater at any time and are therefore not representative of the crater. As described by Pilkington and Grieve [9], craters are surficial features with a minimal depth component, particularly in the outer rim; so it is likely that erosion removed any low density material that may have contributed to a negative gravity anomaly beyond the transient crater. Similarly, no significant topographic features indicate the full extent of the apparent crater. However, the circumferential and radial canyons are interpreted to be the result of fault-channeled erosion and indicate that the crater's structure has a greater AOE than previously thought [2,3,6]. Furthermore, the previously described terraces are interpreted to be bounded by inward-dipping normal faults that can often be identified by the vertical offsets observed in the wedge cross-sections. These features indicate a minimum apparent crater radius, prior to erosion, of ~14 km. When the original presence of over 200 of the Eureka Sound formation is considered [7], we predict that the apparent crater would have extended to at least 15 km and would have risen to a regional plateau ~550 to 600 m above sea level.

**Conclusion:** We conclude that the Haughton Impact Structure has a transient crater diameter of 16 km. The morphology of the excavated crater is defined by a central area of deep excavation, with a diameter of

~2 to 3 km, surrounded by an area of shallow excavation, which occupies the remainder of the transient cavity. Due to the erosive state of the Haughton Impact Structure, previous studies have concluded that the apparent crater diameter is ~24 km. However, based on evidence of the extent of the crater's structural influence, we propose that the original apparent crater diameter is ~30 km. This is consistent with the modified Z-model described by Sharpton and Dressler [8], where Z decays as a function of time. This modified Z-model resolves many of the conflicts [2] with the original Z-model for the Haughton structure described by Redeker and Stoffler [10]. We also define the crater's morphology to contain a central proto-peak ring structure preserved within the crater's subsided area. This indicates that the size of the Haughton Impact structure (~30 km) is within the terrestrial central-structure transition range from a central peak to a peak-ring for a complex impact crater in a sedimentary target.

**References:** [1] Sherlock S. C. et al. (2005) *Meteoritics & Planet. Sci.*, 40, 1777–1787. [2] Hajnal Z. and Scott D. (1988) *JGR*, 93, 11930–11942. [3] Pohl J. et al. (1988) *Meteoritics*, 23, 235–238. [4] Osinski G. R. et al. (2005) *Meteoritics & Planet. Sci.*, 40, Nr 12, 1789–1812. [5] Osinski G. R. and Spray J. G. (2005) *Meteoritics & Planet. Sci.*, 40, Nr 12, 1813–1834. [6] Grieve R. A. F. (1988) *Meteoritics*, 23, 249–254. [7] Hickey L. J. et al. (1988) *Meteoritics*, 23, 221–231. [8] Sharpton V. L. (2003) *Workshop on Impact Cratering*, Abstract #8059. [9] Pilkington M. and Grieve R. A. F. (1992) *Rev. of Geophys.*, 30, 161–181. [10] Redeker H.-J. and Stöffler D. (1988) *Meteoritics*, 23, 185–196.

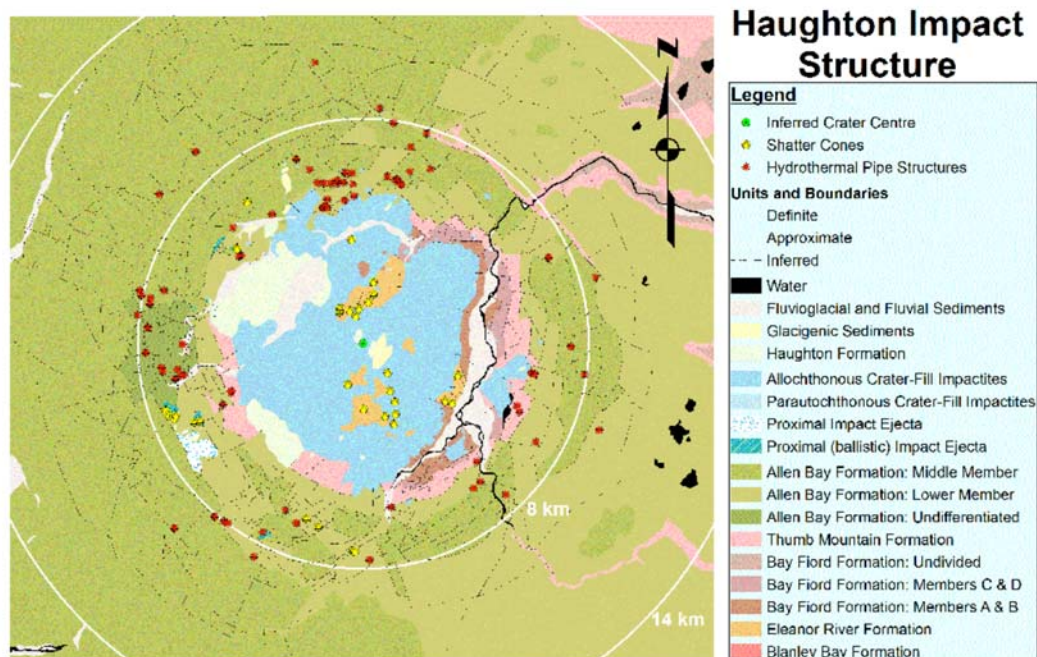


Figure 3. Digitized HIS geological map [4,5].



**IDENTIFYING PARTIALLY CHLORITIZED SMECTITE AT GALE CRATER, MARS.** Sarah E. Perry<sup>1</sup> and Elizabeth B. Rampe<sup>2</sup>, <sup>1</sup>Department of Earth Science and Geogrpahy, Vassar College, Poughkeepsie, NY 12604 (sarperry@vassar.edu) <sup>2</sup>Aerodyne – Jacobs JETS Contract, NASA JSC, Houston, TX 77058

**Introduction:** Clay minerals have been detected on Mars via orbital surveys and rover missions [1,2]. Since these clays are hydrous alteration products of Mars' basaltic crust, their presence gives insight into the planet's aqueous history. Characterizing the clay mineral structures and chemical compositions can provide specific details about formation mechanisms and diagenetic processes.

The most common clay minerals on Mars are smectites and chlorites [1]. Smectite is a swelling clay, whereas chlorite has a brucite- or gibbsite-like interlayer sheet that prevents the structure from expanding. There is also evidence for smectite/chlorite intergrades [3], which may include smectites that have brucite-like pillars within some interlayer sites. CheMin XRD data from JK show a broad 10 Å 001 peak which is indicative of the presence of a collapsed 2:1 smectite. CB has a 13.2 Å 001 peak that is indicative of an expanded smectite [2]. Patterns from both samples have a 4.59 Å 02l peak. This is similar to saponite's 4.56 Å peak. It has been theorized that the 13.2 Å peak at CB may be due to partial chloritization, which prevents the smectite from fully collapsing to 10 Å.

Investigating these intergrades in the laboratory is essential for identifying them on the Martian surface with orbital and landed data and for distinguishing partially chloritized smectite from discrete smectite and chlorite.

Using three types of terrestrial smectites, we created partially chloritized smectites by adding  $Mg^{2+}$  and  $OH^-$  to a clay suspension to produce  $MgOH_2$  pillars. We pillared the smectites to various degrees by altering the  $Mg/OH$  ratio. We chose  $Mg^{2+}$  as the cation because *Curiosity* discovered evidence for early diagenesis in  $Mg$ -bearing fluids in Gale crater [4]. We then collected X-ray diffraction (XRD) and evolved gas analysis (EGA) data using laboratory instruments similar to those on Mars landers and orbiters. These data can be directly compared to data returned from Mars, specifically from the Cumberland (CB) and John Klein (JK) drill sites, to identify and characterize the relative chloritization of the Martian clay mineral intergrades.

**Methods:** Three types of smectite – SWy-1, a montmorillonite from Crook County, NY; NAu-2, a nontronite from Uley Mine, South Australia; and Fe-saponite (griffithite) from Griffith Park, CA – were used as analogs for Mars. Air dried and Na-saturated were analyzed via XRD to ensure purity. Saturation was done according to Moore and Reynolds (1997) [5] by shaking the clays in a 1.0 M Na salt solution for at least 6 hours. The suspension was then centrifuged and

decanted. This was repeated two more times, after which the suspension was washed with distilled water three times.  $Mg$  saturation was also done so the results could be compared to the pillared clays.

We tested different pillaring procedures by varying parameters to determine which combination gave the best results, including the pH of the pure clay suspension, the final pH of the suspension, the concentration of clay in the  $Mg^{2+}$  and  $OH^-$  solution, and the mEq of  $Mg^{2+}$ /gram clay. Our tests were done with a 1.5  $Mg/OH$  ratio because full chloritization should occur at that point [6], with our final tests using a 1.75 ratio to ensure complete chloritization. We heated the samples to 300°C to dehydrate the clays and examine the presence of  $Mg(OH)_2$  pillars with XRD, where samples should remain partially expanded if pillars are present.

Based on these tests, our final procedure involves first creating a well dispersed clay suspension (~17%) and adjusting its pH to ~11 with 1 M NaOH. To this suspension, we added 17 mEq  $MgCl_2$ /gram clay. NaOH (1.5 M) was titrated dropwise until the desired  $Mg/OH$  ratio was achieved. The suspension was stirred for 30 minutes to ensure pillars formed. We centrifuged and decanted the supernatant and then washed the sample once with distilled water to remove soluble salts. The resulting solids were dried at 250 °C until completely dry. This procedure was based off of Xeidakis (1996) [6]. We did this for four different molar  $Mg/OH$  ratios: 1.75, 1.5, 1.0, and 0.5, assuming 1.0 and 0.5 would be partially chloritized and 1.5 and 1.75 fully chloritized.

All samples were run by XRD two times: under ambient conditions and after being placed in an  $N_2$ -purged glove box (~100 ppm  $H_2O$ ) overnight to simulate dry, Mars-like surface conditions. Samples were brought up to the machine in an airtight container and quickly put into the machine and underwent five quick scans to see if rehydration occurred. Measurements were made on oriented clay slides (ambient only) and random powder mounts (ambient and  $N_2$ ) using a Panalytical X'Pert Pro MPD instrument. Scans were collected from 5-30° 2 $\theta$  (Cu-K $\alpha$ ) to measure reflections from basal spacings and 02l peaks and from 58-65° 2 $\theta$  to measure 060 reflections. EGA was also performed using a Labsys Evo with a ThermoStar gas analyzer under conditions similar to the MSL-Sample Analysis at Mars (SAM) instrument (30 mbar pressure, He carrier gas, 30-1000 °C) to measure the release of  $H_2O$  from the dehydration and dehydroxylation of the samples.

**Results:**

**XRD.** Pillared GP diffraction patterns show 14.6–14.5 Å 001 peaks, with smaller d-spacings and intensities at higher OH/Mg ratios (Figure 1a). These d-spacings are slightly smaller than what's observed under air dried conditions (15 Å). All samples have a 1.54 Å 021 peak consistent with air dried GP, while the 1.75 ratio has an additional peak at 1.57 Å. After being exposed to dry N<sub>2(g)</sub>, the 001 peak varies from 14.7–14.1 Å, with smaller d-spacings and intensities at higher ratios.

Pillared NAu-2 001 peaks range from 15–14.5 Å (Figure 1b). The 0.5 ratio has a much larger d-spacing than the others. These peaks are similar to the air dried 15 Å peak. There is a decrease in intensity with higher ratios except for 0.5, which is only slightly more intense than the 1.75 ratio. The 021 peak is at 1.52 Å for all ratios, consistent with air dried NAu-2. After being exposed to dry N<sub>2(g)</sub>, all ratios have a 14.4 Å 001 peak except for 0.5, which is collapsed. Intensity increases at higher ratios, which is the opposite of GP.

Pillared SWy-1 001 peaks range from 15.6–15.2 Å, with a slight shift to smaller d-spacings with higher ratios. The 021 peak is at 1.5 Å, consistent with air dried sample. After being exposed to dry N<sub>2(g)</sub>, the 0.5 ratio had a 13.3 Å 001 peak while the rest were at 14.7 Å. There was no trend in peak intensity with OH/Mg ratio (Figure 1c).

Samples with OH/Mg ratios of 1.75 were heated to 300°C to completely dehydrate the samples and examine whether complete chloritization occurred. The 001 peaks of all three samples decreased in intensity and shifted to slightly smaller d-values (Figure 2a & b).

**EGA.** EGA data for mass 18 of the GP samples show dehydroxylation occurring between 100–150, ~450, and 700°C for the 0.5 and 1.0 ratios (Figure 3). Pure GP has a similar pattern but the high temperature evolution occurs at 750 °C. The 450°C peak intensity increases and the 150°C peak decreases with higher ratios. At ratios 1.5 and 1.75 – where we expected full chloritization to occur – the 450°C peak broadens and H<sub>2</sub>O evolution starts occurring at 320°C. EGA data for the SWy-1 and NAu-2 samples are still being gathered.

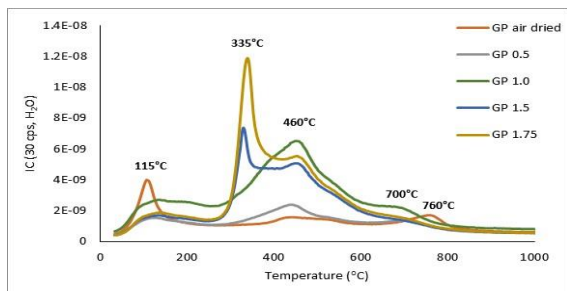


Figure 3. EGA H<sub>2</sub>O data under SAM-like conditions for air dried, 0.5, 1.0, 1.5, and 1.75 Mg/OH ratios.

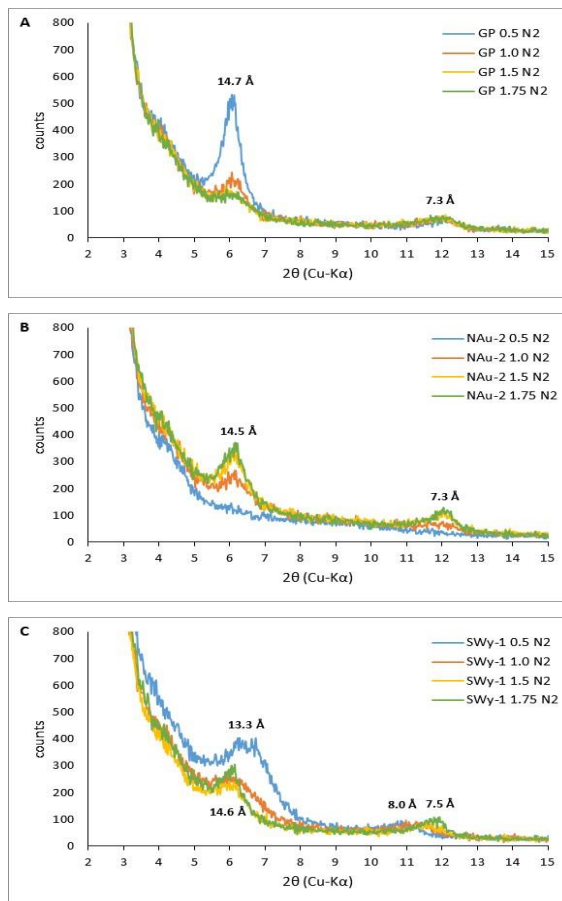


Figure 1. XRD data for (A) GP, (B) NAu-2, and (C) SWy-1 smectites after being in N<sub>2</sub> overnight.

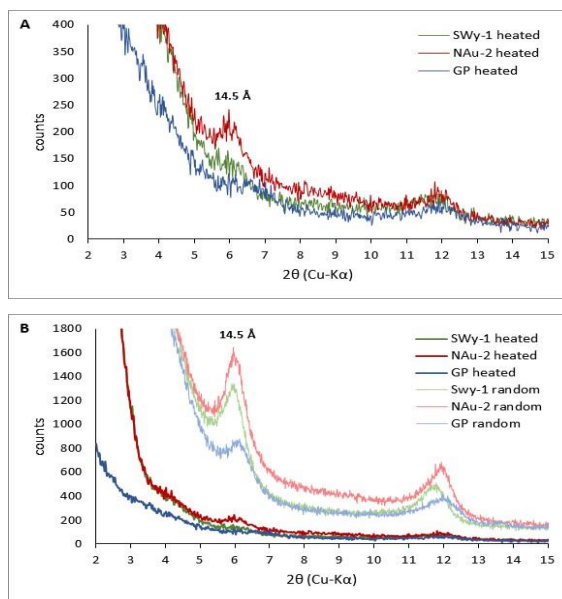


Figure 2. XRD data for heated 1.75 ratio clays (A) compared to non-heated (B).



### Discussion:

**XRD.** Contrary to what we expected, complete chloritization did not occur in our laboratory samples with OH/Mg ratios of 1.75. We do not know the degree to which each sample is pillared with  $\text{Mg}(\text{OH})_2$ ; however, because complete collapse did not occur when exposed to dry  $\text{N}_{2(g)}$ , the smectites were likely pillared to some degree. Mg/OH pillaring slightly decreases the smectite's d-spacing, but none collapsed to 13.2 Å. Under Mars-like conditions the d-spacings decreased to 14.7-14.1 Å, but only the 0.5 ratio of SWy-1 had a peak close to the one seen at Cumberland (13.3 Å). When comparing our patterns to those collected by *Curiosity's* CheMin of the Cumberland data, we suggest that minimal pillaring could explain the 001 phyllosilicate peak at 13.2 Å.

**EGA.** For griffithite, the 150°C  $\text{H}_2\text{O}$  evolution corresponds to the loss of  $\text{H}_2\text{O}$  in the interlayer site and ~750°C is the dehydroxylation of the octahedral sheet. In partially chloritized griffithite, the 450°C evolution is likely from the dehydroxylation of the  $\text{Mg}(\text{OH})_2$  pillars in the interlayer site. For the 0.5 and 1.0 ratios, the increased intensity of the 450°C peak at higher Mg/OH ratios, coupled with decreased 150°C intensity, is indicative of the formation of  $\text{MgOH}_2$  pillars and the decrease of free  $\text{H}_2\text{O}$  in the interlayer site. The 1.5 and 1.75 ratios also have a high intensity 450°C peak, indicating pillaring, but the origin of the 320°C evolution is not known. Ideally, these two ratios would have had a pattern similar to chlorite ( $\text{H}_2\text{O}$  evolution occurring ~750°C).

SAM  $\text{H}_2\text{O}$  EGA data at both CB and JK shows a broad low temperature peak terminating at ~450°C and somewhat-broad high temperature peak near 750°C (Figure 2). This is similar to the pattern for griffithite [7]. Partially chloritized griffithite (0.5 and 1.0 ratios) has a pattern similar to griffithite with varying peak intensities. There is no evidence that pillaring griffithite gives the broad, ~450°C peak shown at CB and JK.

**Conclusions:** Although our laboratory experiments did not produce fully chloritized smectite, we produced partially chloritized smectite. XRD analysis consistently shows peaks at 14.7-14.1 Å when measured after exposure to dry  $\text{N}_{2(g)}$ , regardless of the degree of pillaring, except for the SWy-1's 13.3 Å peak at the 0.5 ratio. Griffithite EGA data for the 0.5 and 1.0 ratios have the same pattern as pure griffithite albeit with different intensities due to the presence of pillars. The unique XRD patterns from Cumberland and John Klein may be consistent with minimal pillaring (ie. 0.5 ratio SWy-1) but more data is needed to confirm. EGA data from pillared griffithite does not seem to be consistent with CB or JK.

**References:** [1] Ehlmann, B. L. et al. (2013). Geochemical consequences of widespread clay mineral formation in Mars' ancient crust. *Space Science Reviews*, 174(1-4), 329-364. [2] Vaniman, D.T. et al. (2014). Mineralogy of a mudstone at Yellowknife Bay, Gale Crater, Mars. *Science*, 343(6169), 1243480. [3] Bristow, T. F. et al. (2015). The origin and implications of clay minerals from Yellowknife Bay, Gale Crater, Mars. *American Mineralogist*, 100(4), 824-836. [4] L  veill  , R.J. et al. (2014). Chemistry of fracture-filling raised ridges in Yellowknife Bay, Gale Crater: Window into past aqueous activity and habitability on Mars. *Journal of Geophysical Research: Planets*, 119(11), 2398-2415. [5] Moore, D. M., and Reynolds, R. C. (1997). X-ray diffraction and the identification and analysis of clay minerals. Oxford: Oxford University Press. [6] Xeidakis, G. S. (1996). Stabilization of swelling clays by  $\text{Mg}(\text{OH})_2$ . Changes in clay properties after addition of Mg-hydroxide. *Engineering geology*, 44(1), 107-120. [7] McAdam, A.C. et al. (2014). SAM-like evolved gas analyses of phyllosilicate minerals and applications to SAM analyses of the Sheepbed Mudstone, Gale Crater, Mars. *LPSC XLV*, Abstract

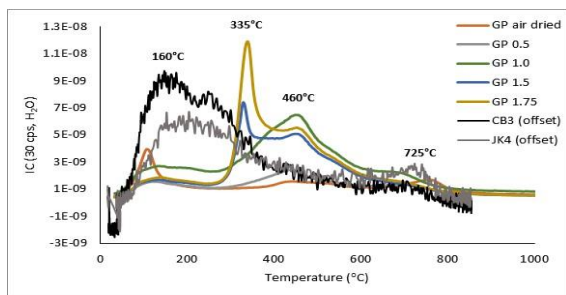


Figure 4. EGA-MS  $\text{H}_2\text{O}$  data from Cumberland and John Klein drill sites compared to  $\text{MgOH}_2$  pillaring experiments. Mass 19 is plotted for CB and JK while mass 18 is plotted for the experiments.

**GEOLOGICAL MAP OF THE HUMBOLDTIANUM BASIN AND ITS DEPOSITS.** E. F. Schmidt<sup>1</sup> and P. D. Spudis<sup>2</sup>, <sup>1</sup>Department of Physics, Embry-Riddle Aeronautical University, 3700 Willow Creek Rd., Prescott, AZ 86301 (schmide2@my.erau.edu), <sup>2</sup>Lunar and Planetary Institute, 3600 Bay Area Blvd., Houston, TX 77058

**Introduction:** Humboldtianum basin is a Nectarian-age multi-ring basin centered at approximately 57° N, 82° E. The inner ring is roughly 275 km in diameter and the outer ring is estimated at around 650 km in diameter [1]. Although the basin was previously studied and mapped [2], new image data from Lunar Reconnaissance Orbiter (LRO) and chemical and mineral concentration data from Clementine and Lunar Prospector provide improved surface image resolution and information on the composition of basin deposits, allowing updated and improved maps to be compiled and new inferences made on the composition of basin ejecta and its crustal target.

The basin is asymmetric and morphologically complex. The area to the south and west of the basin is similar to other lunar basins but the area to the north and east does not have a well-defined outer ring. Bel'kovich crater appears to overlie Humboldtianum's inner ring in this area. The unusual shape of the basin may indicate its formation from an oblique impact, as has been proposed for some other basins [3].

The purpose of this project was to create a geological map centered on the Humboldtianum basin, allowing a better understanding of the composition of its ejecta deposits and crustal target. In addition, due to its

age, compositional analysis was used to help determine the level of influence of the younger Imbrium and Crisium ejecta on Humboldtianum itself. This was done by mapping all the important units related to the basin, which included their relative ages, and looking for compositional clues as to their origin. The image data for this map came from narrow-angle and wide-angle Lunar Reconnaissance Orbiter Cameras (LROC), the LRO GLD-100 topographic map [4], along with data on TiO<sub>2</sub> and FeO content from Clementine images [5] and thorium concentration data from Lunar Prospector [6]. This map can be used to help future lunar mission planning and in determining the basin target composition. In addition, this new map may help develop a better understanding of how Bel'kovich and Humboldtianum are related.

**Methods:** Basin-centered orthographically projected LRO images and topographic maps were used in ArcGIS 10.1 to assist in the determination and mapping of the different stratigraphic units around the basin based on relative age, elevation changes, surface texture, albedo, FeO content (to help distinguish between plains and mare), and position. To improve comparisons and provide continuity with existing maps, mapping conventions were based on those used in the 1978 USGS map of the lunar north side [2]. Only craters of greater than 20 km in diameter were included in the map allowing the focus to remain on the basin-related units.

After the new map was finished, compositional maps were overlaid onto it, allowing for the concentrations of Fe, Ti, and Th to be determined for each geological unit and region of the basin and its surrounding area.

**Results:** A total of 23 geological units were mapped (Fig. 1). The units were divided into four categories: basin materials, other terra materials, mare and dark mantle materials, and crater deposits.

The basin materials were subdivided into five units, Nectarian-age massifs (Nbma) – high, mountainous areas that denote the location of the inner basin ring, approximately 125 km to 150 km from the basin center; Humboldtianum basin floor material (Nbf); basin lineated material (Nbl) – material with lineations oriented radially to the basin center around Humboldtianum believed to have been formed by the deposition of basin ejecta, Nbl extends between 210 km and 320 km from the outer edge of the basin; Imbrium basin lineated material (Ibl) – lineated material thought to be ejection

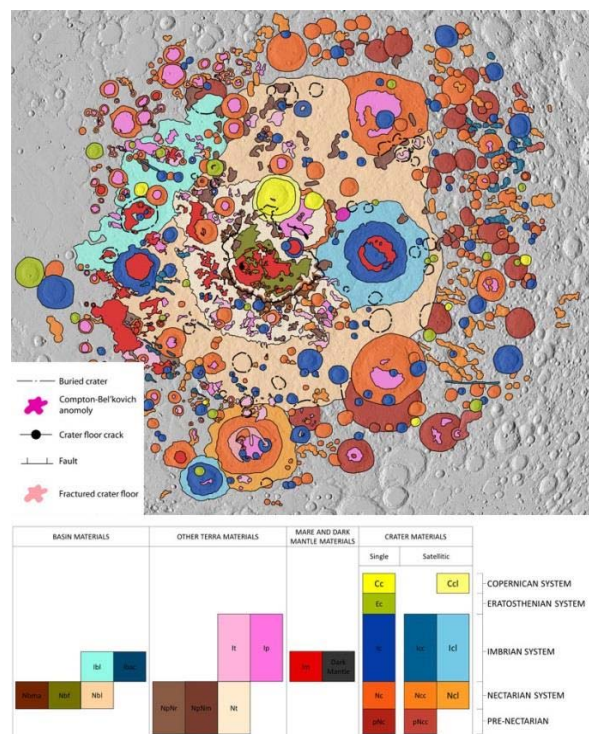


Figure 1 – New geological map of the Humboldtianum basin.

ta from the basin impact, located about 2000 km to the northwest; Imbrium basin secondaries (Ibsc) – secondary craters from the Imbrium impact, these are primarily crater chains oriented radially to the center of the Imbrium basin.

Other terra materials were subdivided into five units, Nectarian and pre-Nectarian rugged material (NpNr) – hilly, rugged terrain, lower in relative elevation than the massifs; Nectarian and pre-Nectarian massifs (NpNm) – massifs, similar to Nbma in appearance but do not exist as part of the inner basin ring; Nectarian terra material (Nt) – slightly smoother, but hilly, older material; Imbrian terra material (It) – light, hummocky surface material; Imbrian plains material (Ip) – light, flat, and smooth, similar in texture to mare but with higher albedo and lower FeO content. Some of these older terra units may be related to the Humboldtianum basin, but lacked diagnostic features to map them as such.

Mare and dark mantle materials were subdivided into two units, Imbrian mare (Im) – smooth, flat surface with very low albedo and high FeO; dark mantle – very low albedo material inside the inner basin ring, found in small quantities around floor-fractured craters, containing high FeO.

Crater materials were subdivided into eleven units including craters and crater chains from pre-Nectarian, Nectarian, Imbrian, Eratosthenian, and Copernican ages. This category also contains lineated material similar to Nbl and Ibl but from non-basin craters around Humboldtianum.

In addition, important non-stratigraphic geologic features were mapped, including large cracks in the Bel'kovich floor, the fault indicating the outer edge of

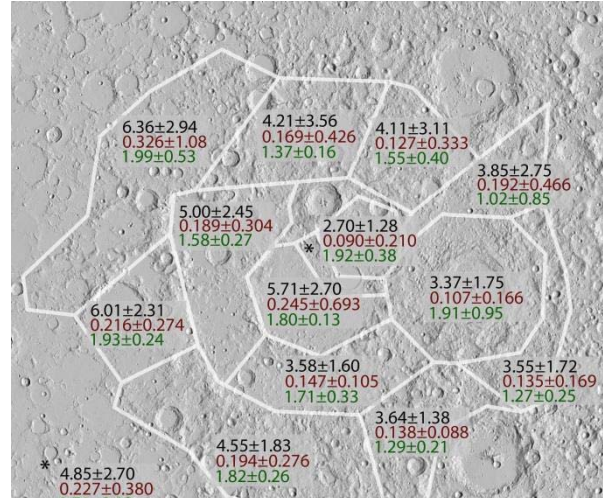


Figure 2 – Regional mineral weight %. Black: FeO, Red: TiO<sub>2</sub>, Green: Thorium (ppm). Uncertainties indicate  $\pm 1\sigma$

the basin, the Compton-Bel'kovich thorium anomaly, and craters buried by basin and other crater ejecta.

The results of the chemical composition data are shown in Figure 2 and Table 1 below. Figure 2 shows the concentration of Fe, Ti, and Th by region around the basin. Table 1 contains the chemical concentrations of the units around the basin.

**Analysis:** Based on the data from Figure 2, although the uncertainties are large, a general negative gradient in FeO content can be seen from the northwest to the south-east, where the region mapped as Imbrium ejecta is the highest in Fe (most mafic). This indicates a slightly larger influence from Imbrium than is detectable from the mapping in Figure 1.

Geologic Unit	FeO wt % $\pm 1\sigma$	TiO <sub>2</sub> wt % $\pm 1\sigma$	Th ppm $\pm 1\sigma$
Bel'kovich Terra Material (Nt)	2.70 $\pm$ 1.28	0.09 $\pm$ 0.21	1.92 $\pm$ 0.38
Bel'kovich Rim (Ne)	3.55 $\pm$ 2.26	0.16 $\pm$ 0.37	2.31 $\pm$ 0.82
Compton-Bel'kovich Anomaly	4.09 $\pm$ 0.88	0.07 $\pm$ 0.06	5.10 $\pm$ 0.19
Compton Lineated Ejecta (Icl)	3.37 $\pm$ 1.75	0.11 $\pm$ 0.17	1.91 $\pm$ 0.95
Fractured Crater Floors	4.82 $\pm$ 1.52	0.20 $\pm$ 0.08	1.58 $\pm$ 0.27
Dark Mantle in Basin	8.43 $\pm$ 3.00	0.34 $\pm$ 0.23	1.91 $\pm$ 0.05
Entire Basin Interior to the Basin Lineated Material*	4.64 $\pm$ 2.48	0.19 $\pm$ 0.26	1.65 $\pm$ 0.27
Hahn Lineated Ejecta (Icl)	6.05 $\pm$ 0.89	0.26 $\pm$ 0.07	1.57 $\pm$ 0.11
Inner Basin Terra Material (Nt)	4.85 $\pm$ 2.70	0.23 $\pm$ 0.38	1.71 $\pm$ 0.12
Inner Basin Rim (Nbma)	4.18 $\pm$ 2.72	0.21 $\pm$ 0.26	1.59 $\pm$ 0.10
Imbrian Plains Material (Ip)**	5.02 $\pm$ 2.40	0.19 $\pm$ 1.31	2.03 $\pm$ 0.76
Imbrian Terra Material (It)**	4.73 $\pm$ 2.00	0.21 $\pm$ 0.30	1.69 $\pm$ 0.31
Mare (Im)**	9.12 $\pm$ 2.79	0.33 $\pm$ 0.32	1.99 $\pm$ 0.40
Humboldtianum Basin Floor (Nbf)	5.71 $\pm$ 2.70	0.24 $\pm$ 0.16	1.80 $\pm$ 0.13
Massifs (NpNm)**	4.02 $\pm$ 3.04	0.22 $\pm$ 0.69	1.50 $\pm$ 0.42

Table 1 – Table of the average mineral concentrations of different units around the basin. For simplicity, this table does not include the regions indicated in Figure 2.

\* Only includes basin-related units, therefore it excludes mare, Imbrian plains material, craters, etc...

\*\* Not all material from indicated units for FeO and TiO<sub>2</sub> are included. Excluded areas contain bad satellite data due to low-angle light in the northern section of the mapped region.



However, due to the formation of subsequent large craters and mare flooding in the area, it is difficult to determine if this high FeO wt % is due solely to Imbrium ejecta or if there is some other cause.

Although there is also a general negative trend in thorium concentrations heading east, a spike can be seen in the Compton ejecta and in the Bel'kovich region. This is caused by the Compton-Bel'kovich thorium anomaly, marked in Figure 1, which has a very high thorium content relative to the rest of the basin region (see Table 1). This feature has been proposed as the site of the eruption of silicic volcanic rocks (i.e. rhyolite), a very rare phenomenon on the Moon [7].

Other than the high concentrations of FeO in the dark mantle and mare, the other units are all of feldspathic highlands composition, with little variation. Compared with the composition of the other basins previously studied [8-11], Humboldtianum ejecta is low in FeO, even lower than Orientale, which is very iron-poor (Fig. 3). This result suggests that the ejecta from Humboldtianum is extremely feldspathic and the basin crustal target likely consisted of very ancient anorthositic rocks, which appear common in the northern central far side highlands [12].

The  $\text{TiO}_2$  content of the ejecta is fairly uniform throughout the region with the two notable exceptions of Compton-Bel'kovich and the terra material (Nt) inside Bel'kovich. The low concentration of  $\text{TiO}_2$  inside Bel'kovich could be related to the influence of the thorium anomaly approximately 100 km away.

The average elevation south of the basin is much higher than the average elevation north of it such that the peaks of the northern massifs are approximately equal in elevation as the southern highlands. Moreover, many massifs exist in the northern areas but not in the southern. One possible explanation for this relation is that the basin-forming impact hit at an oblique angle pointing in a northerly direction. It should be noted that the highest elevation in the south is approximately the same as the peaks of the massifs in the north.

Compared with other recently mapped basins, Imbrium, Orientale, and Crisium [9-11], Humboldtianum contains lower levels of Ti and, on average, lower levels of Fe (Fig. 3). Notably, impact melts were not found during the mapping process. This is either because they do not exist or they do exist but are now covered by younger impact materials.

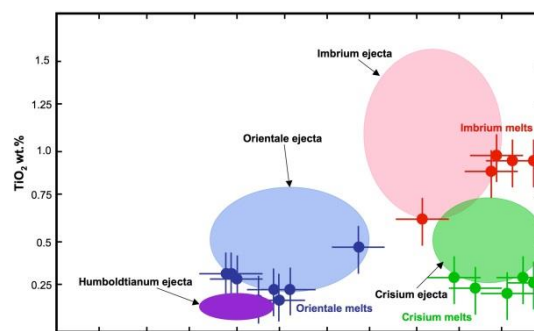


Figure 3 – Composition comparison between recently mapped lunar basins. After [8-11]

**Conclusions:** A new geological map of the Humboldtianum basin was created using new data from the LRO, Clementine, and Lunar Prospector missions. The chemical data was overlaid onto the geographic map and related to mapped ejecta units around the basin, and stratigraphic units were recorded and analyzed.

The compositional analysis shows that the different units had similar mineral content. However, there was a noticeable difference in FeO content in the different regions of the basin, a negative content gradient was found to exist from the north-west to the south-east. This indicates that there is a large Imbrium influence on that side of the basin but much less, if any, influence on the side of Humboldtianum basin away from Imbrium.

It was also found that large massifs are found north of the basin while the region to the south is more uniform in elevation, with fewer massifs present in the area.

**References:** [1] Wilhelms, D. E. (1987) *The Geologic History of the Moon*. USGS Prof. Paper 1348, 302 pp. [2] Lucchitta, B. K. USGS map I-1062. [3] Schultz, P. H., Crawford, D. A. (2016) doi:10.1038/nature18278 [4] Scholten, F. et al. (2012) doi:10.1029/2011je003926 [5] Lucey P.G. et al. (2000) JGR 105, 20297. [6] Lawrence D. et al. (2007) GRL 34, L03201, doi:10.1029/2006GL028530. [7] Jolliff, B. L. et al. (2011) LPSC. [8] Smith, M. C., Spudis, P. D. (2013) LPSC. [9] Martin, D. J. P., Spudis, P. D. (2014) LPSC [10] Murl, J. N., Spudis, P. D. (2015) LPSC [11] Sliz, M. U., Spudis, P. D. (2016) LPSC. [12] Jolliff, B. L. et al. (2000) JGR 105, 4197.



## LPI Summer Intern Program in Planetary Science-Orientation

June 6







### JSC Stardust Lab and Lunar Curation Tour

Stardust, a NASA Discovery-class mission, was the first to return samples from a comet and from interstellar space.

Lunar Curation - The facility consists of storage vaults for the samples, laboratories for sample preparation and study, a vault for sample data and records, and machinery to supply nitrogen to the cabinets in which the samples are stored and processed.

June 6



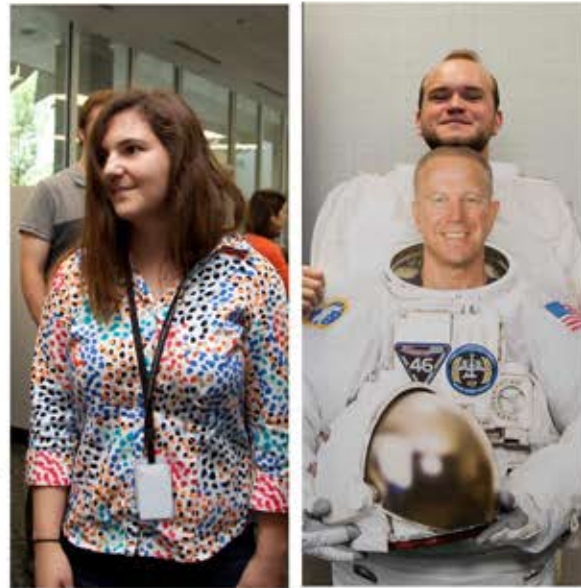




NASA's Christopher C. Kraft, Jr. Mission Control Center (MCC-H), also known by its radio callsign, Houston, is the facility at the Lyndon B. Johnson Space Center in Houston, Texas that manages flight control for America's human space program, currently involving astronauts aboard the International Space Station (ISS)

Historic Mission Control Located in Building 30 of the Johnson Space Center, this is the facility where NASA monitored nine Gemini and all Apollo missions, including the historic Apollo 11 trip to the moon.

June 14







The Robotic Systems Technology Branch is responsible for the research, engineering, development, integration, and application of robotic hardware and software technologies for specific flight and ground robotic system applications in support of human spaceflight.

The Modular Robotic Vehicle (MRV) is a vehicle designed for transportation in congested areas. The MRV was designed without a central power plant, transmission, fuel tank, and direct mechanical linkages between driver input devices and the actuators used to accelerate, brake and/or steer the car. Interns were given an interactive demonstration of the MRV. An experience of a life time.

July 22







Meteorite Tour The curation and collection of Antarctic meteorites is a U.S. funded, cooperative effort among NASA, the National Science Foundation (NSF) and the Smithsonian Institution. Meteorites of greater interest and undergoing detailed study are kept at JSC for distribution to the scientific community, but irons are sent directly to the Smithsonian Institution.

July 26







Dr. Don Pettit is one of the most productive scientist-astronauts in the agency. He is the fourth most experienced American spacefarer of all time, with two long-duration stays aboard the International Space Station and a Space Shuttle mission. Don has also engaged in a six-week expedition to collect meteorites in Antarctica.





Ice Cream Social - July 19



Ice Cream Social - July 19



Sky Fest - Juno mission to Jupiter - August 6



USRA Employee, Family, and LPI Summer Intern BBQ - August 8



Murder Mystery Party - July 9



Murder Mystery Party - July 9



Sky Fest - Juno mission to Jupiter - August 6



Find the Most Scientifically Inaccurate Things in the Movie, 'The Core' June 23